



Die Grenzen der  
Chemie neu ausloten?  
It takes  
#HumanChemistry

Wir suchen kreative Chemikerinnen und Chemiker,  
die mit uns gemeinsam neue Wege gehen wollen –  
mit Fachwissen, Unternehmertum und Kreativität für  
innovative Lösungen. Informieren Sie sich unter:

[evonik.de/karriere](https://evonik.de/karriere)

# Global Alignment of Carbon Nanotubes via High Precision Microfluidic Dead-End Filtration

Christian Rust, Han Li, Georgy Gordeev, Manuel Spari, Markus Guttmann, Qihao Jin, Stephanie Reich, and Benjamin S. Flavel\*

Single wall carbon nanotubes (SWCNTs) dispersed by negatively charged sodium deoxycholate (DOC) or positively charged cetrimonium bromide (CTAB) are shown to assemble into aligned films (3.8 cm<sup>2</sup>) on polycarbonate membranes by slow flow dead-end filtration. Global alignment ( $S_{2D \max} \approx 0.85$ ) is obtained on both pristine polyvinylpyrrolidone (PVP) coated membranes and those with an intentional 150–600 nm groove pattern from hot embossing. In all cases, a custom microfluidic setup capable of precise control and measurement of the volume rate, transmembrane pressure, and the filtration resistance is used to follow SWCNT film formation. Conditions associated with the formation of SWCNT crystallites or their global alignment are identified and these are discussed in terms of membrane fouling and the interaction potential between the surface of the membrane and nanotubes. SWCNT alignment is characterized by cross-polarized microscopy, atomic force microscopy, scanning electron microscopy (SEM), and Raman spectroscopy.

## 1. Introduction

Single-wall carbon nanotubes (SWCNTs) are a quasi 1D allotrope of carbon with outstanding but highly anisotropic electronic, mechanical, thermal and optical properties.<sup>[1]</sup> In addition, the various 1D structural arrangements of carbon atoms in a SWCNT, described by the chiral indices (n, m), bestow SWCNTs with the ability to be either metallic (m) or semiconducting (s) and provide diameter dependent absorption bands in the infrared, visible and ultra-violet spectral regions.<sup>[2]</sup> Consequently, SWCNTs can be found in multiple research fields such as energy,<sup>[2b,3]</sup> photonics,<sup>[4]</sup> electronics<sup>[5]</sup> and medicine,<sup>[6]</sup> but their hierarchical organization over a large surface area (i.e., wafer scale) remains a grand challenge to device application.

Accordingly, ever since their discovery, significant effort has been directed toward forming SWCNT thin films with in-plane (axial) alignment. Aligned films are expected to provide performance enhancements<sup>[7]</sup> and in some cases even establish new material properties not seen in their disordered counterparts,<sup>[8]</sup> leading to potential applications like terahertz polarizers<sup>[9]</sup> and air-stable n-type transistors.<sup>[10]</sup>

Methods to achieve in-plane SWCNT alignment include: dry shear of vertically grown forests and mis-aligned films<sup>[11]</sup> or the use of faceted nano-steps on a miscut sapphire surface to direct growth,<sup>[12]</sup> but difficulties to control the chiral type have limited their application. Alternatively, the Langmuir-Blodgett technique,<sup>[13]</sup> evaporation induced self-assembly,<sup>[14]</sup> the use of magnetic and electric fields,<sup>[15]</sup> stretching of polymers,<sup>[16]</sup> and solution shear of highly concentrated superacid or nanotubide dispersions<sup>[17]</sup> have allowed for the use of sorted nanotubes but the small surface area covered and the necessity to remove strong dopants has likewise limited their appeal. Highly selective separation techniques have been developed in organic and aqueous solvents and these provide precise control of the diameter,<sup>[18]</sup> length,<sup>[19]</sup> wall-number,<sup>[20]</sup> electronic property,<sup>[21]</sup> chirality,<sup>[22]</sup> and enantiomeric type.<sup>[23]</sup> For organic-based separations, recent work by Jinkins et al.<sup>[24]</sup> stands out because confined shear<sup>[25]</sup> was used to align polymer dispersed SWCNTs on a 100 cm<sup>2</sup> substrate. Alternatively, aqueous-based dispersions provide the greatest flexibility to arbitrarily select single chiral SWCNTs<sup>[3f,26]</sup> and work by He et al.<sup>[27]</sup> to use vacuum filtration to align them


C. Rust, H. Li, M. Spari, B. S. Flavel  
Institute of Nanotechnology  
Karlsruhe Institute of Technology  
Hermann-von-Helmholtz-Platz 1, 76344 Eggenstein-Leopoldshafen,  
Germany  
E-mail: benjamin.flavel@kit.edu

C. Rust  
Institute of Materials Science  
Technische Universität Darmstadt  
Alarich-Weiss-Straße 2, 64287 Darmstadt, Germany

G. Gordeev, S. Reich  
Department of Physics  
Freie Universität Berlin  
Arnimallee 14, 14195 Berlin, Germany

M. Guttmann  
Institute of Microstructure Technology  
Karlsruhe Institute of Technology  
Hermann-von-Helmholtz-Platz 1, 76344 Eggenstein-Leopoldshafen,  
Germany

Q. Jin  
Light Technology Institute  
Karlsruhe Institute of Technology  
Engesserstraße 13, 76131 Karlsruhe, Germany

 The ORCID identification number(s) for the author(s) of this article can be found under <https://doi.org/10.1002/adfm.202107411>.

© 2021 The Authors. Advanced Functional Materials published by Wiley-VCH GmbH. This is an open access article under the terms of the Creative Commons Attribution License, which permits use, distribution and reproduction in any medium, provided the original work is properly cited.

DOI: 10.1002/adfm.202107411

is especially promising. Although they were not the first to observe alignment via filtration, the high nematic order, high packing density ( $3.8 \times 10^5$  SWCNTs  $\mu\text{m}^{-2}$ ) and the wafer-scale dimension of their films led to their work receiving significant attention.

In general, filtration is a mechanical separation process, in which an impermeable species (in this case SWCNTs) in a solution (feed) moves toward a membrane by convective transport. These species are then either collected on the membrane (retentate) or pass it (permeate). This is described by a ratio known as the retention, which is usually defined by the molecular weight of the impermeable species and the membrane itself. The enrichment of species in the retentate is in turn described by two phenomena; concentration polarization and fouling. Concentration polarization is the loose accumulation of mass on the surface of a membrane.<sup>[28]</sup> This layer can be removed by rinsing or back-flushing and is thus reversible. Conversely, fouling describes the formation of a solid, irreversible layer on the membrane<sup>[28,29]</sup> and it is undesirable for most applications. Indeed, industrial processes aim to improve the usable lifetime of a membrane by operating in the concentration polarization regime and applying successive rinsing and back-flushing steps.<sup>[30]</sup> For cross-flow filtration, in which the feed is passed parallel to the membrane surface and where mass is constantly being added and removed from its surface, concentration polarization is conventionally defined by a critical flow-rate, below which no fouling is observed.<sup>[28,31]</sup> For dead-end filtration, the feed approaches the membrane perpendicular to the surface and this results in an unavoidable mass accumulation. In this case, concentration polarization occurs below a critical permeate volume and depends on the flow-rate used.<sup>[29b]</sup> For volumes larger than the critical permeate volume, fouling will always be inevitable for dead-end filtration.

Experimentally, the two filtration regimes can be identified by monitoring the resistance of the membrane during passage of the feed with respect to the permeated volume. Fouling is identified as a positive gradient in the resistance.<sup>[32]</sup> The resistance can be determined by knowledge of the flow rate and in situ measurement of the transmembrane pressure ( $p_{\text{TMP}}$ ), which is defined as the difference of pressure on the feed ( $p_{\text{in}}$ ) and permeate ( $p_{\text{out}}$ ) sides of the membrane. Additionally, analysis of the gradient of the resistance with respect to permeated volume allows for the mode of fouling to be determined, or in other words, the way in which mass accumulates on the membrane.<sup>[33]</sup> This is done by applying so called blocking laws which were first introduced by Hermans and Bredée,<sup>[34]</sup> further improved by Gonsalves and Grace<sup>[35]</sup> and were later summarized by Hermia et al.<sup>[36]</sup> in a simple power law expression. Eventually, Hlavacek and Bouchet derived these laws for constant flow-rate experiments.<sup>[37]</sup>

In early work by Shaffer et al.<sup>[38]</sup> it was recognized that enrichment of carbon nanotubes at the membrane surface can result in the formation of a nematic phase and self-ordered domains of multiwalled CNTs were reported. He et al.<sup>[27]</sup> later suggested that the carbon nanotubes self-orientate in a 2D plane of minimum potential above the surface of the membrane. This plane of minimum potential is a consequence of attractive van-der Waals forces and repulsive electric double-layer forces being superimposed. McLean et al.<sup>[39]</sup> used DLVO theory to calculate the distance of this minimum to the mem-

brane surface by approximating the carbon nanotubes as spherical particles, and recently Wu et al.<sup>[40]</sup> refined those calculations by considering them as cylindrical objects. Obviously, the total mass of SWCNTs to be filtered will determine whether or not a nematic phase ( $\approx 4$  mg mL<sup>-1</sup><sup>[41]</sup>) is formed, but Dan et al.<sup>[42]</sup> and King and Panchapakesan<sup>[43]</sup> later discussed the importance of a slow flow rate and surprisingly, a low nanotube concentration in the feed solution to nematic ordering. This was later rationalized as the required rotation time for an unaligned CNT to orientate itself as it approaches the surface. The remarkable discovery made by He et al.<sup>[27]</sup> was that under very specific filtration conditions it was possible to obtain a single globally aligned domain of SWCNTs. However, the key question of what drives the transformation of domains to global alignment remains a matter of debate. Recently, Komatsu et al.<sup>[44]</sup> have shown that the global alignment direction is closely correlated to a series of macro- and micro-grooves in the polycarbonate track-etched (PCTE) membrane, all of which have a common direction and are present from a process used by the manufacturer. Correspondingly, the authors later intentionally emboss the membrane with a series of periodically spaced grooves<sup>[45]</sup> using a diffraction grating and show that there is an enhancement in alignment. Alternatively, Walker et al. concluded that the grooves are not the most important aspect for alignment but rather a directional charging of the surface, which can be further enhanced by tribo-charging the membrane.<sup>[46]</sup> Nevertheless, it is commonly agreed upon that alignment occurs near to, but not directly on the membrane surface.<sup>[27,39,43,44,46]</sup>

Global alignment has been shown for polyvinylpyrrolidone (PVP) coated PCTE membranes with a pore size of 80 nm or 200 nm and a filtration diameter of 15 mm.<sup>[27,44]</sup> In all cases, the SWCNTs were dispersed by negatively charged surfactants such as sodium deoxycholate (DOC) or sodium dodecylbenzenesulfonate (SDBS) and at a concentration ( $\approx 0.004$ – $0.03$  wt %) well below the critical micelle concentration (0.24 wt % for DOC<sup>[27]</sup> and 0.13 wt % for SDBS<sup>[47]</sup>) of the surfactant. A total volume of 4–5 mL with a SWCNT concentration of  $\approx 8$ – $15$   $\mu\text{g mL}^{-1}$ <sup>[27,46,48]</sup> was then used in a filtration process that was described by He et al.<sup>[27]</sup> as being “well controlled and at a slow speed”. In practice, this involves a series of steps from zero to gentle pressure at the beginning of filtration such that volume rates of 1–2.5 mL h<sup>-1</sup> are obtained, followed by a reduction to 0.5 mL h<sup>-1</sup> as the SWCNTs begin to enrich, and a final ramp to  $\approx 10$  mL h<sup>-1</sup> which is applied when the solution is 3–5 mm above the membrane surface in order to dry the film. While He et al. emphasized the importance of the initial stabilization of the flow, Komatsu et al. later stated that the pushing step had to be optimized in order for the nanotubes to globally align.<sup>[27,44]</sup>

Unfortunately, and despite the efforts of the authors to provide complete experimental information, the filtration technique remains challenging to reproduce, and most research groups anecdotally report the formation of domains but no global alignment. Primarily, the difficulty to reproduce global alignment is associated with the experimental sophistication required to control the flow rate with high precision, but also because it is unclear how narrow the set of flow conditions are, or which of the filtration steps are crucial. These issues are further complicated by the desire to report a general technique, capable of aligning all types of carbon nanotubes on a broad range of membranes. However, in practice, the experimental

conditions are varied for different diameter CNTs/membrane combinations and only films with champion alignment are presented. For example, large diameter ( $d_t \approx 1.4$  nm) carbon nanotubes are also found to align better than small diameter ( $d_t \approx 0.73$ – $1$  nm) with  $S_{2D}$  values of  $\approx 0.90$  and  $\approx 0.74$  reported, respectively.<sup>[27,46]</sup>

In order to better understand the requirements for global alignment, precise filtration control and accurate in situ measurement of carbon nanotube film formation are required. In this direction, Walker et al.<sup>[46]</sup> built an automated and parallelized filtration setup that uses machine vision to measure the flow rate. In our work, we use a calibrated positive pressure microfluidic dead-end filtration setup that is capable of in situ measurements of  $p_{TMP}$ , volume rate and membrane retention. This allows us to vary the volume rate of filtration with high accuracy ( $\pm 1.7 \mu\text{L min}^{-1}$  at  $100 \mu\text{L min}^{-1}$ ) and identify regimes associated with the formation of SWCNT domains with varying degrees of alignment and enables us to elucidate the importance of each step of the filtration process. This discussion is informed by resistance measurements of membranes with pore sizes ranging from 50 to 200 nm, the corresponding resistance curve during film formation; zeta potential measurements of both the membrane and the SWCNT dispersion; the concentration or total mass of the SWCNTs filtered, and the influence of hot embossing on the alignment mechanism.

## 2. Results and Discussion

In the past, global alignment of SWCNTs has been performed on membranes supported by a glass or metallic frit, to which a glass funnel is clamped from above and a rubber stopcock used to seal the setup to a Buechner flask. A vacuum pump is then connected to apply a controllable under-pressure and regulate the flow rate of filtration.<sup>[27,43,44,46]</sup> However, despite its convenience, such a setup does not allow for a direct inline measurement of  $p_{TMP}$  and retention, nor does it provide accurate initial conditions. Even in the absence of the applied under-pressure, a capillary force and gravity still act on the feed solution to draw it into the membrane, and up to several hundred microliters may already have passed before the vacuum pump is switched on. If the beginning of the filtration is key to global alignment,<sup>[27]</sup> then a highly accurate flow control has to be initiated from a zero-flow state.

To circumvent these issues, we built a custom microfluidic positive-pressure dead-end filtration cell. A technical drawing of the components in expanded view is shown in **Figure 1A** and a cross-section of the assembled cell is shown in **Figure 1B**. In this design, the membrane is supported by a  $300 \mu\text{m}$  fine stainless-steel mesh laser-welded to a  $0.2$  mm thick metal ring with an inner diameter of  $22$  mm and outer diameter matching the membranes used ( $47$  mm). The inner diameter defines the effective filtration area ( $3.8 \text{ cm}^2$ ) and represents the largest to date.<sup>[27,44,46]</sup> Teflon blocks are pressed on either side of the membrane holder and these are held in place inside a stainless-steel sleeve by two flanges. The first flange fixes the membrane in place and allows for the addition of feed solution through the top, whilst the second makes a gas-tight seal for filtration. The assembled cell is placed inline as shown in **Figure 1C** by connecting the inlet and outlet of the stainless-steel sleeve via

$1/4$ "-28 UNF standard threads and  $1/8$ " and  $1/16$ " polytetrafluoroethylene (PTFE) or polyether ether ketone (PEEK) tubing with an internal diameter of  $2$  mm and  $1$  mm, respectively. Positive pressure is provided through the inlet by a Nitrogen gas bottle connected to an electronic pressure regulator rated to  $0$ – $2$  bar operation. The outlet of the filtration cell is met by an arrangement of two  $3/2$  solenoid valves, which can be actuated to pass the permeate either through a high- ( $\pm 2$  bar), low- ( $\pm 340$  mbar) pressure piezoelectric sensor or stop the flow completely. After the pressure sensors, the permeate passes into a Coriolis flow sensor followed by a UV-diode array detector and finally into a waste container. A bubble catcher avoids artifacts in the pressure and flow measurements<sup>[49]</sup> and comparison of time resolved absorption spectra with and without a membrane, allow for the determination of membrane retention.<sup>[50]</sup> The gravity flow of the system without a membrane in place and with the solenoid valve open was adjusted to a constant value of  $100 \mu\text{L min}^{-1}$  by raising or lowering the position of the waste container relative to the height of the filter holder. In this way, the fluid flow driven by gravity in the setup was hindered by the backpressure of the water in the waste bottle with respect to its relative height to the filtration cell.

A detailed description of the procedure used to calibrate the pressure sensors, load a fresh membrane and the method to control the volume rate can be found in the Supporting Information (SI). Importantly, the pressure regulator ( $p_{in}$ , process variable) was controlled by a feedback loop minimizing the error between the actual flow and the desired flow (setpoint) from the Coriolis sensor. Additionally, the initial zero flow state was afforded by the ability to fill the dead volume under the membrane in the filtration cell, the pores of the membrane itself, and the tubing leading up to a solenoid valve (in a closed position) prior to adding SWCNTs. The transmembrane pressure  $p_{TMP}$  was calculated as the difference between the measured pressure at the sensor in the gas regulator,  $p_{in}$  and one of the inline piezoelectric sensors,  $p_{out}$ . As an example, **Figure 1D** shows the data obtained from the setup for an entire filtration experiment. Throughout the remainder of the discussion, it will be customary to consider only specific sections of the filtration labeled as slow and fast filtration in order to improve the clarity of the presentation.

In general a filtration process can be characterized by Darcy's law<sup>[32]</sup>

$$R_{\text{total}} = \frac{p_{\text{TMP}}}{\mu J} \quad (1)$$

where  $\mu$  is the viscosity of the solvent ( $\text{H}_2\text{O}$ ) and  $J$  the fluid flux, which can be calculated as the volume rate,  $\dot{v} = \frac{dV}{dt}$ , normalized by the membrane area  $A_m$ .  $R_{\text{total}}$  is a series of resistances, many of which accumulate during filtration<sup>[51]</sup>

$$R_{\text{total}} = R_{\text{setup}} + R_m + R_{\text{cp}} + R_b \quad (2)$$

$R_{\text{setup}}$  is associated with the components used in the filtration setup and it is often neglected because it is minor compared to the other resistances. We account for it by the aforementioned calibration of the piezoelectric sensors, which effectively



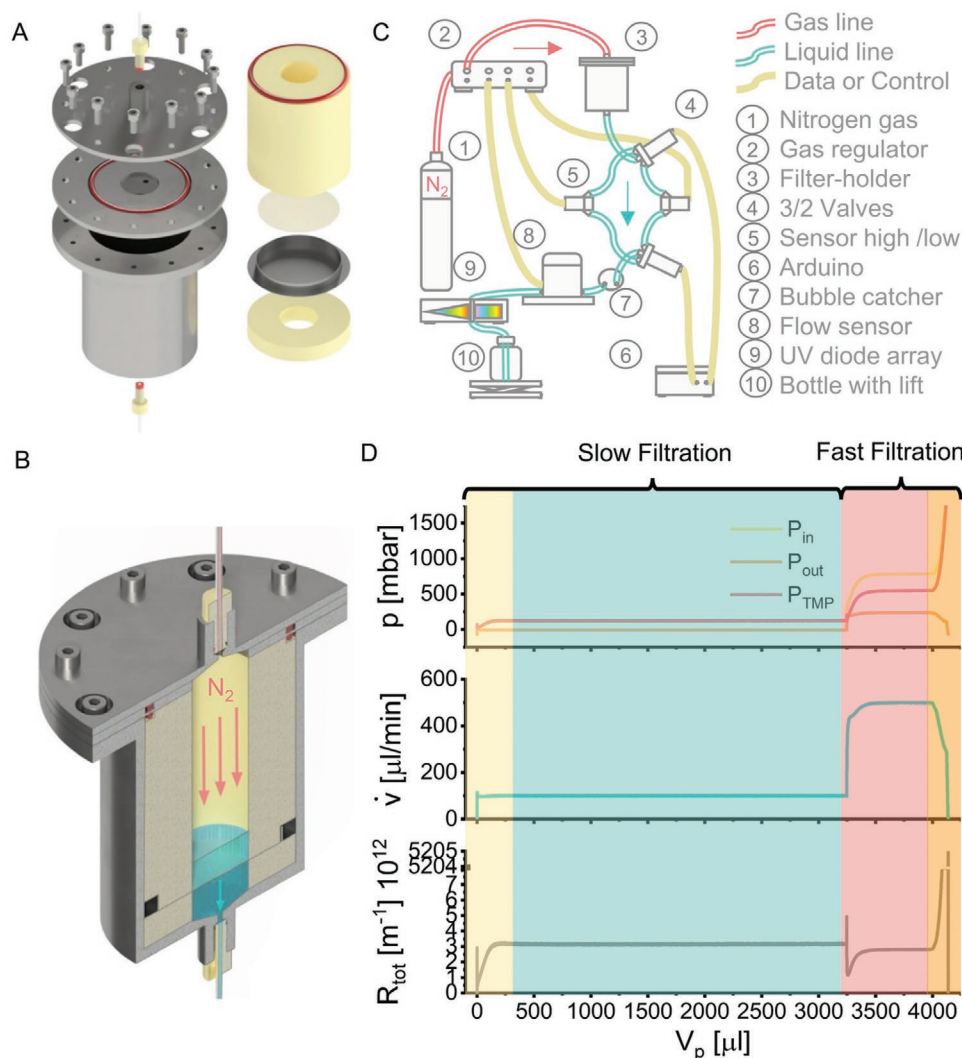


**Figure 1.** A) Expanded view of the filtration holder showing the internal components (right) and the stainless-steel sleeve (left). B) Cross-sectional view of the assembled holder. C) Schematic of the complete microfluidic dead-end filtration setup. D) Filtration data divided into color-coded regions: concentration polarization (yellow), film growth (blue), a push phase (red), and drying (orange).

sets  $p_{\text{TMP}} = 0$  for a setup absent of a membrane and filled with water.  $R_m$  is the membrane resistance and it depends on the pore size, porosity and thickness of the membrane as well as its surface charge or wettability.  $R_{\text{cp}}$  is the resistance increase due to concentration polarization and  $R_b$  describes the resistance increase due to irreversible fouling. It is  $R_b$  that can be used in combination with blocking laws to understand the formation of the SWCNT film during alignment. By fitting a power law to the resistance, one can identify one of four possible mechanisms for CNTs to accumulate at the membrane surface. These are 1) complete blocking, 2) intermediate blocking, 3) standard blocking, and 4) cake filtration. A schematic along with the associated equations can be found in Figure S2 in the Supporting Information.

In this work, polycarbonate membranes coated and uncoated (UC) with a PVP layer and with 50 nm, 80 nm, 100 nm and 200 nm pore size were used. To measure  $R_m$ , 4 mL of deionized water (pH = 6.93) was filtered through each membrane at

volume rates of 40–150  $\mu\text{L min}^{-1}$ , Figure S3A in the Supporting Information, and the average value taken at a permeate volume of 3.25 mL, Figure 2A. Also shown is an 80 nm membrane after hot embossing (HE) but this will be discussed later. Using an approach outlined in Figure S4 in the Supporting Information, these values were compared to the theoretical membrane resistance,  $R_{m_t}$ , for membranes with a uniform pore length,  $l_m$  and diameter,  $d_{\text{pore}}$ . It can be seen that the theoretical value is always lower than the measured value. This can be attributed to some pores not being straight and the added resistance due to the impermeable parts of the membrane as well as its zeta potential in the case of a real membrane.<sup>[52]</sup>

Figure 2B shows the zeta potential measured across the surface of the membranes,  $\zeta_{\text{surf}}$ , for the pH range 4–10. In agreement with previous studies on polymer surfaces,<sup>[53]</sup> hydrophobic membranes (the UC membranes) were found to have a lower zeta potential compared to hydrophilic membranes (PVP coated membranes) ( $\approx -95$  mV versus  $\approx -60$  mV at pH = 6.93)

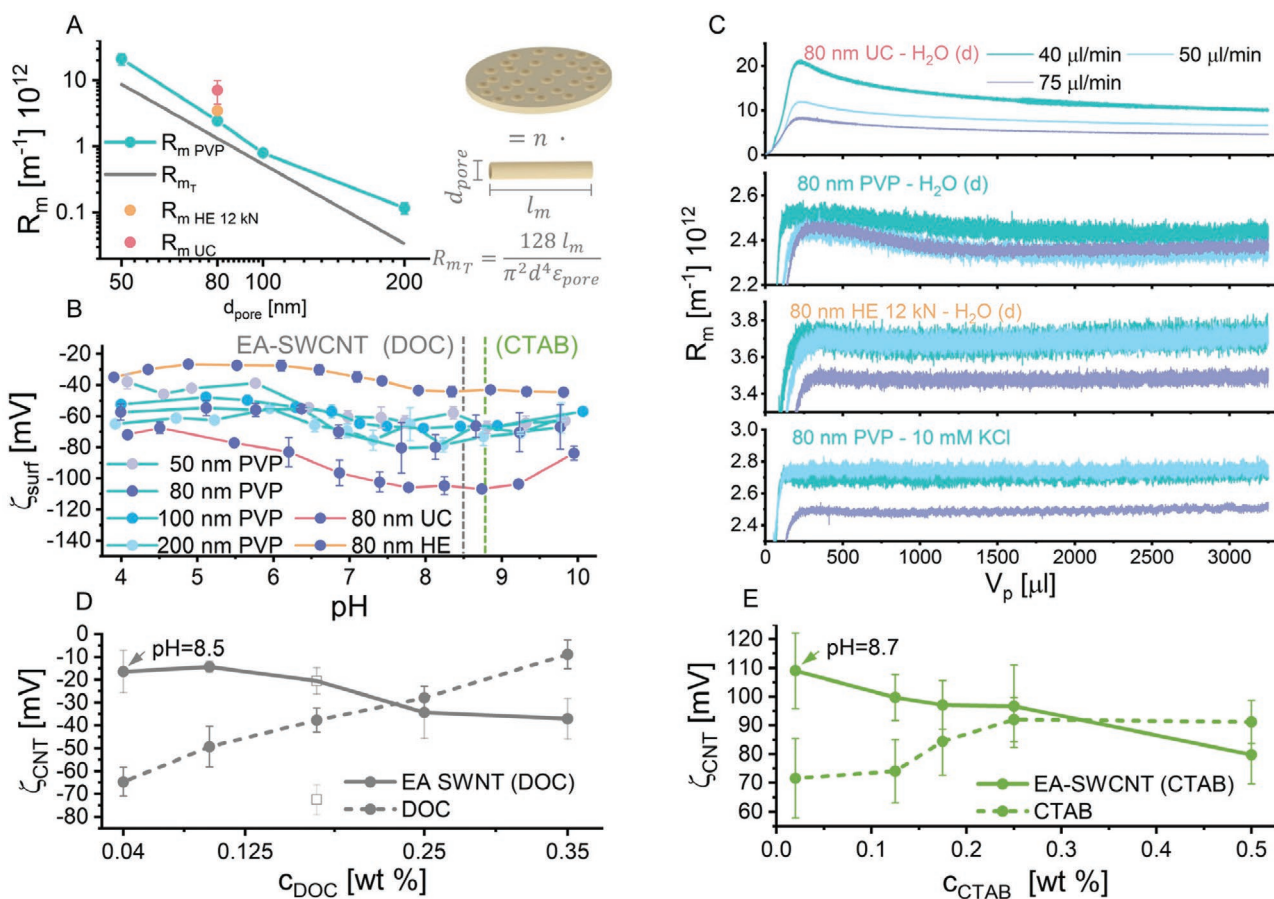


**Figure 2.** A) Experimental and theoretical values of the membrane resistance ( $R_m$ ). B) Surface zeta potential ( $\zeta_{\text{surf}}$ ) of PVP coated and uncoated (UC) membranes and PVP coated membranes after hot embossing (HE). C) Volume evolution of  $R_m$  for various 80 nm membranes in either deionized water or  $10 \times 10^{-3}$  M KCl. Zeta potential with and without  $8 \mu\text{g mL}^{-1}$  of EA-SWCNTs in either D) DOC or E) CTAB.

and this resulted in a considerably higher  $R_m$  for the UC membranes. For example,  $R_m = 7.09 \times 10^{12} \text{ m}^{-1}$  versus  $2.43 \times 10^{12} \text{ m}^{-1}$  for an UC versus PVP coated 80 nm membrane. As expected, due to  $\zeta_{\text{surf}}$  being a surface sensitive parameter it was not found to be dependent on the pore size of the membrane. In contrast, the zeta potential measured through the pores,  $\zeta_{\text{pore}}$ , varied with the pore diameter, Figure S5 (Supporting Information).

Figure 2C shows the volume evolution of  $R_m$  for an 80 nm membrane with a total permeate volume ( $V_p$ ) of 3.25 mL of either deionized water or  $10 \times 10^{-3}$  M KCl. For all membranes measured in deionized water,  $R_m$  reaches a maximum soon after filtration begins ( $\approx 275 \mu\text{L}$ ) and then stabilizes to the value used in Figure 2A. The initial increase in resistance is likely due to a timing mismatch between the regulator sensor and the inline pressure sensor. As such, the resistance values are reliable only after  $\approx 275 \mu\text{L}$ . The membrane resistance  $R_m$  is often-reported to be a constant,<sup>[54]</sup> but certain effects can lead to a change in membrane resistance over time. Calvo et. al reported that polycarbonate track etched membranes tend to swell after the first contact with water, changing their morphology, opening up more pores and increasing in thickness, which could explain the decrease of resistance over time.<sup>[55]</sup> The in-line spectrometer was used to exclude the possibility that this decay in  $R_m$  was due to the removal of the PVP by

deionized water. Only trace amounts of PVP were detected and indeed the largest initial peak and decay in  $R_m$  was observed for the UC membrane, Figure S3 (Supporting Information). It can also be seen that the maximum resistance corresponds well to the absolute surface zeta potential, and we propose that the change in resistance might also be connected to the formation of an electric double layer. Previously, it has been reported that adding salt to an SWCNT dispersion hinders their alignment<sup>[46]</sup> due to a screening of the surface potential. Indeed, for a  $10 \times 10^{-3}$  M KCl solution, this initial decay was not observed. On the contrary, adding DOC (0.04–0.35 wt %) did not suppress the peak and decay, Figure S3B in the Supporting Information, albeit a higher  $R_m$  could be observed.

Zeta potential measurements were also performed on the electric arc (EA)-SWCNTs used in this work, Figure 2D,E. These had an average diameter of  $1.4 \text{ nm}$  and were dispersed in either DOC or Cetrimonium bromide (CTAB), with an average length of  $691 \pm 471$  and  $844 \pm 471 \text{ nm}$ , respectively. He et al. reported an average tube length of  $227 \text{ nm}$ , while Walker et al. stated a range between 200 and 400 nm for similar tubes using DOC as surfactant.<sup>[27,46]</sup> We consider longer tubes to have an advantage in terms of additional attractive van der Waal forces, aiding in the formation of crystallites, whereas shorter tubes would be easier to rotate. Atomic force microscopy (AFM) imaging revealed that



most CNTs were individualized and that the centrifugation step removed most of the bent or distorted tubes. Further information on their absorption spectrum and the calculation of concentration can be found in Figure S6 in the Supporting Information. In the absence of EA-SWCNTs, the zeta potential increases linearly with surfactant concentration. This has been explained as an effect related to the formation of micelles at higher concentrations that shield the real zeta potential of a single surfactant molecule.<sup>[56]</sup> In the presence of EA-SWCNTs, the absolute zeta potential,  $\zeta_{\text{CNT}}$ , was found to decrease with increasing surfactant concentration. All proceeding experiments were performed with DOC dispersions at a concentration of 0.04 wt % and this corresponds to a  $\zeta_{\text{CNT}}$  of  $-14$  mV. The zeta potential of a colloidal solution is often considered to indicate its stability and values between  $\pm 15$  mV are usually considered to be unstable.<sup>[57]</sup> This is the case for DOC based dispersions below 0.1 wt % and corresponds to the concentration range that Walker et al.<sup>[46]</sup> found best for alignment. Alternatively, the zeta potential for CTAB dispersed EA-SWCNTs decreased from  $+90$  mV at 0.25 wt % surfactant content to  $+72$  mV at 0.125 wt %. This places all of the dispersions in a regime of stability, even at low surfactant concentration, Figure 2D. In light of the results presented later, we conclude that an instable dispersion is not needed, but rather

that the SWCNT walls should be depleted of surfactant. Complete zeta potential measurements can be found in Figure S7 in the Supporting Information.

Figure 3A shows a series of slow filtration experiments using 4 mL of an  $8 \mu\text{g mL}^{-1}$  dispersion of EA-SWCNTs with 0.04 wt % DOC at volume rates of  $25\text{--}125 \mu\text{L min}^{-1}$  on an 80 nm membrane.  $R_b + R_{\text{cp}}$  was calculated by subtracting  $R_m$  from  $R_{\text{tot}}$ . Immediately apparent is a resistance peak during the initial  $\approx 500 \mu\text{L}$  of filtration that was largest for a flow rate of  $25 \mu\text{L min}^{-1}$ , reached a minimum at  $100 \mu\text{L min}^{-1}$  and then increased for  $125 \mu\text{L min}^{-1}$ . In agreement with the discussion of Figure 2C, the peak is attributed to the membrane itself rather than the SWCNTs and is therefore not considered in the following discussion. In Figure 3A, the concentration polarization regime has been shaded in color for each volume rate. This is the region prior to an observable increase in the resistance, i.e., before fouling occurs. At  $25 \mu\text{L min}^{-1}$  and  $50 \mu\text{L min}^{-1}$  no increase in  $R_b + R_{\text{cp}}$  was observed and this implies that the critical volume ( $V_c$ ) for fouling exceeds 3.25 mL at these volume rates. Here it is important to state that the retention of the membrane was measured to be 0.98, Figure S8 (Supporting Information). Therefore, the possibility for SWCNTs to simply pass through the membrane and thereby not increase

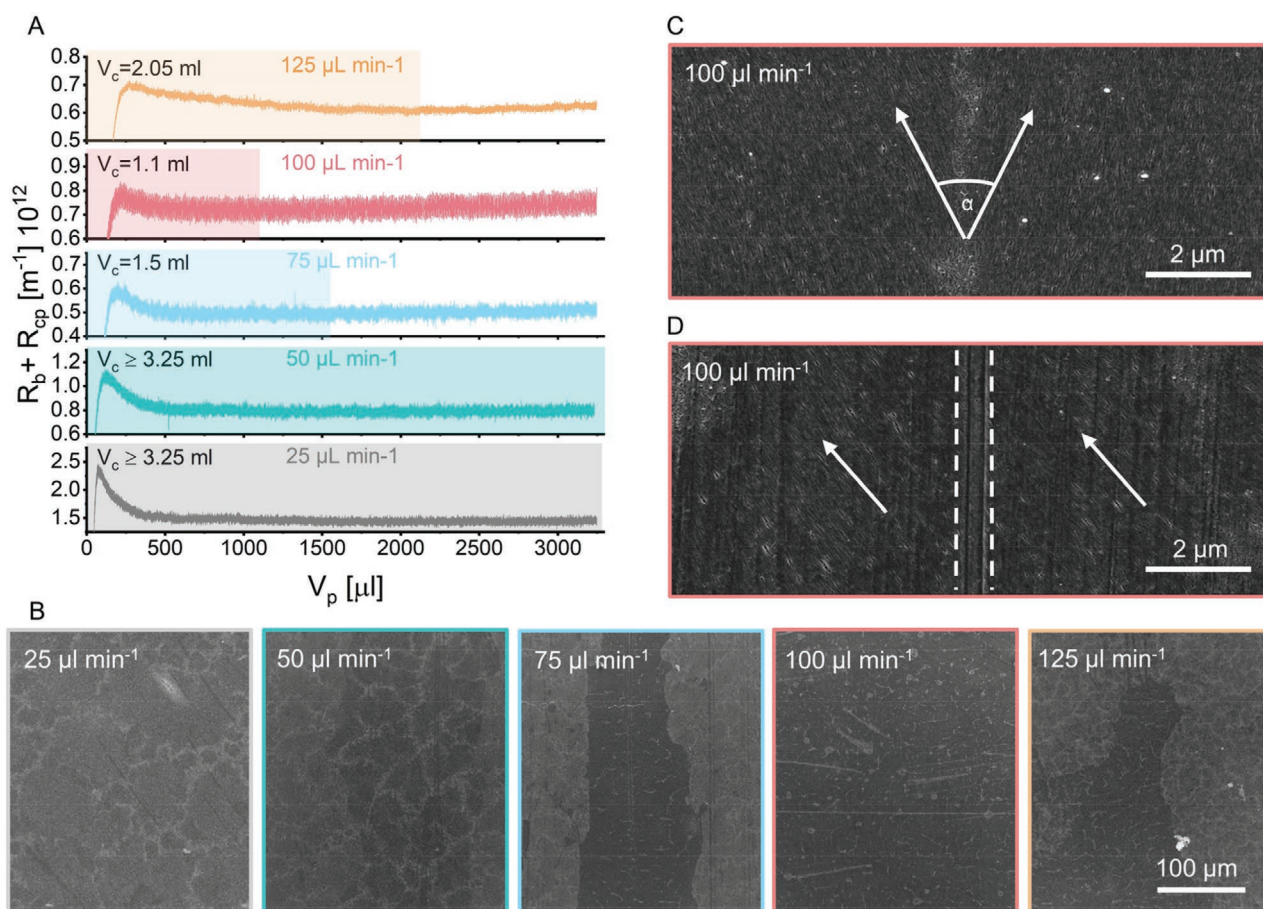


**Figure 3.** A) Resistance measured during slow filtration of 4 mL of an  $8 \mu\text{g mL}^{-1}$  dispersion of EA-SWCNTs with 0.04 wt % DOC at volume rates of  $25\text{--}125 \mu\text{L min}^{-1}$  on an 80 nm membrane. B) SEM images of the SWCNT film (transferred to a silicon wafer) obtained at these volume rates with C) an enlarged view of the  $100 \mu\text{L min}^{-1}$  film showing mis-aligned SWCNT crystallites. D) A SWCNT domain with an alignment direction (arrows) offset from that of a groove (dashed lines) in the membrane. Note: Finer grooves can also be seen in the image and these have not been highlighted.

the measured resistance can be excluded. In this regime, the SWCNTs reaching the surface gather in a dispersed state above the membrane.<sup>[58]</sup> Alternatively, for 75  $\mu\text{L min}^{-1}$ , 100  $\mu\text{L min}^{-1}$  and 125  $\mu\text{L min}^{-1}$ , the resistance was found to increase after 1.5 mL, 1.1 mL and 2.05 mL, respectively. In all cases the resistance increase was found to be linear and this corresponds to the cake filtration mode of fouling, Figure S2 in the Supporting Information.<sup>[58]</sup>

Representative SEM images with constant imaging parameters of the film obtained for each volume rate are shown in Figure 3B. In all cases, the films were transferred to silicon wafers such that the SWCNTs shown are those between the membrane and retentate (bottom layer). For reference, regions containing densely packed and aligned SWCNTs appear dark in contrast, whereas disoriented and less dense regions appear bright. Large SWCNT crystallites are visible at 25  $\mu\text{L min}^{-1}$  and these were found to become more compact with increasing volume rate, until the entire membrane was covered with a dense film at 100  $\mu\text{L min}^{-1}$ . At 125  $\mu\text{L min}^{-1}$ , this trend is reversed and less dense areas comparable to 75  $\mu\text{L min}^{-1}$  were observed. An increase in the critical volume was also found to occur at this volume rate. In all images, the thin regions of brighter contrast correspond to grain boundaries consisting of disordered SWCNTs, which divide crystallites at a small angle to each other and an example is shown for 100  $\mu\text{L min}^{-1}$  in Figure 3C. Similar results were obtained for the 50, 100, and 200 nm pore size membranes and total resistance curves taken during filtration for these membranes can be found in Figure S9 in the Supporting Information.

Cross-polarized microscopy and machine vision were used to evaluate the size and shape of these crystallites, Figures S10–S13 in the Supporting Information. Interestingly, it was found that the average size of the crystallites generally decreased with increasing volume rate for all membranes tested, Figures S14 and S15 (Supporting Information). For the 80 nm membrane, the shape of the crystallites also changed from round at 50  $\mu\text{L min}^{-1}$  to a mixture of round and elongated domains at 75  $\mu\text{L min}^{-1}$ , to entirely elongated crystallites at 100  $\mu\text{L min}^{-1}$ , Figure S11 (Supporting Information). This corresponds to the crossing point between filtrations with only concentration polarization and those with concentration polarization and cake formation. The same effect was also observed for the 50 nm membrane albeit at different volume rates, Figure S14 (Supporting Information). For the 200 nm membrane, the slowest volume rate obtainable with our setup already resulted in elongated domains, whilst for the 100 nm membranes a mixture of round and elongated domains was always observed and this was independent of the volume rate used. Although the crystallites were most often found to be orientated with the direction of the grooves, occasionally, they were also found to be mis-aligned, Figure 3D, which suggests that macro- and micro-grooves in the membrane do not function as a structural template for SWCNT alignment. For an 80 nm membrane with DOC dispersed SWCNTs, 100  $\mu\text{L min}^{-1}$  was concluded to provide the best conditions for alignment, but at this stage, still with many misaligned crystallites. Apart from variations in the optimum flow rate (50 nm: 70  $\mu\text{L min}^{-1}$ , 100 nm: 150  $\mu\text{L min}^{-1}$ , 200 nm: 95  $\mu\text{L min}^{-1}$ ), the best alignment was always obtained when the concentration polarization regime was the shortest,

Figures S10–S13 (Supporting Information). Previously, He et al.<sup>[27]</sup> have stated that the initial flow determines whether or not the nanotubes form an aligned film, and we can now interpret this to be the volume rate with the smallest critical volume,  $V_c$ .

These experiments were repeated for 4 mL of an 8  $\mu\text{g mL}^{-1}$  dispersion of EA-SWCNTs in 0.02 wt % CTAB, Figure S16 (Supporting Information). This is the first time that a positively charged surfactant has been investigated for SWCNT alignment. Despite the lower critical volume, the measured resistance curves show a similar behavior to that of the DOC dispersed SWCNTs for volume rates up to 50  $\mu\text{L min}^{-1}$ . At higher volume rates, first an initial increase in resistance is observed, followed by a plateau and then the usual decrease in resistance leading up to fouling. Essentially, this implies that at first rapid fouling occurs; this is followed by concentration polarization and then a secondary fouling step. For all volume rates greater than 25  $\mu\text{L min}^{-1}$  a compact film of SWCNTs was observed and above 50  $\mu\text{L min}^{-1}$  a unidirectionally aligned film without grains was obtained. Corresponding cross-polarized microscopy images are shown in Figure S17 in the Supporting Information. At first glance, this can easily be confused with a globally aligned SWCNT film. However, upon examination of tears in the film, it can be seen that this first aligned layer is followed by a disordered layer of SWCNTs, Figure S16D in the Supporting Information. Interestingly, cross-polarized microscopy images of the top side of the SWCNT film (still on the membrane) reveal that the SWCNTs start to align again at the top, forming a third layer, Figure S18 (Supporting Information). For CTAB dispersed SWCNTs a disordered layer is sandwiched between two aligned films.

In an attempt to improve the alignment of the DOC dispersed SWCNTs, we next varied the volume rate of the fast filtration step. This was performed with 750  $\mu\text{L}$  of feed solution still in the filtration cell in order to homogeneously cover the membrane. Volume rates of 300–700  $\mu\text{L min}^{-1}$  were tested. Figure S19A in the Supporting Information shows the resistance  $R_b + R_{cp}$  measured for a 3.25 mL feed of an 8  $\mu\text{g mL}^{-1}$  dispersion of EA-SWCNTs with 0.04 wt % DOC filtered onto an 80 nm membrane using a constant slow filtration step of 100  $\mu\text{L min}^{-1}$ . The sharp increase in resistance at  $\approx 3.25$  mL is related to drying of the film and the linear increase after an initial rise at  $\approx 2.75$  mL shows a caking behavior resulting from further compression of the film. Regardless of the push step applied, the absolute value of the resistance with respect to the volume rate did not follow any trend nor was it found to have an impact on the quality of alignment. This is demonstrated by almost indistinguishable cross-polarized images in Figure S19B in the Supporting Information for push speeds of 700, 500, and 300  $\mu\text{L min}^{-1}$ . This was also true for experiments with CTAB, Figure S20 (Supporting Information).

Walker et al.<sup>[46]</sup> previously reported that the meniscus formed during this last stage of the filtration can lead to the formation of spherulites and used a hydrophobic silane coating on their glass funnel to avoid them.<sup>[46]</sup> Our experimental setup used hydrophobic PTFE and polycarbonate cylinders with contact angles of  $\approx 115^\circ$  and  $\approx 88^\circ$ , respectively.<sup>[59]</sup> This afforded us with a slightly convex meniscus and we were unable to identify the formation of spherulites. Instead, we observed the formation of drying rings, Figure S21A,B (Supporting Information).



The diameter of the drying rings was found to be dependent on the push step and increased with the volume rate for all membranes, regardless of their pore size, Figure S21C (Supporting Information). A diameter of 22 mm corresponded to the area of filtration and was thus considered to be a SWCNT film without drying rings. Therefore, in all proceeding experiments, the push step was adjusted to be the lowest volume rate (i.e.,  $500 \mu\text{L min}^{-1}$  for an 80 nm membrane) resulting in a film free of drying rings. For the 50 nm membrane, the maximum output pressure of 2 bar was not sufficient to avoid the drying rings and instead a volume rate of  $200 \mu\text{L min}^{-1}$  was used.

The role of filtered mass on the global alignment of SWCNTs was then investigated by varying the feed volume in 1 mL steps. All other parameters were held constant:  $8 \mu\text{g mL}^{-1}$  dispersion of EA-SWCNTs with 0.04 wt % DOC on an 80 nm membrane with a  $100 \mu\text{L min}^{-1}$  filtration step to a final volume of 750  $\mu\text{L}$  followed by push step of  $500 \mu\text{L min}^{-1}$ . These films were transferred to a silicon wafer and their topography was measured by AFM, Figure 4A and Figure S22 (Supporting Information). Intuitively, a linear increase in film thickness might be expected

for increasing SWCNT mass. Instead, analysis of AFM height profile data, revealed the existence of a plateau at  $\approx 62 \text{ nm}$  for masses of 16–24  $\mu\text{g}$ , Figure 4B. The same plateau was observed for experiments with CTAB dispersed SWCNTs, Figure S21 (Supporting Information).

To further investigate this phenomenon, the masses used above were diluted in deionized water in order to fill the total capacity of the filter holder (20 mL). This effectively varied the concentration of the SWCNTs to be  $0.4\text{--}1.6 \mu\text{g mL}^{-1}$  and DOC to be  $0.002\text{--}0.016 \text{ wt}\%$ . The cake resistance measured for a  $100 \mu\text{L min}^{-1}$  filtration step of these dispersions is shown in Figure 4C. It can be seen the increase in resistance after concentration polarization became visually more apparent than what was seen previously in Figure 3A. For the 24  $\mu\text{g}$  sample, the initial increase in resistance was now best fit by an intermediate blocking mode of fouling after a critical volume of 6.3 mL and later ( $V_p = 13.5 \text{ mL}$ , see black arrow) changed to cake filtration. This is in agreement with work by Nakamura et al.<sup>[51b]</sup> who state that intermediate blocking is always followed by cake filtration once the membrane becomes fully

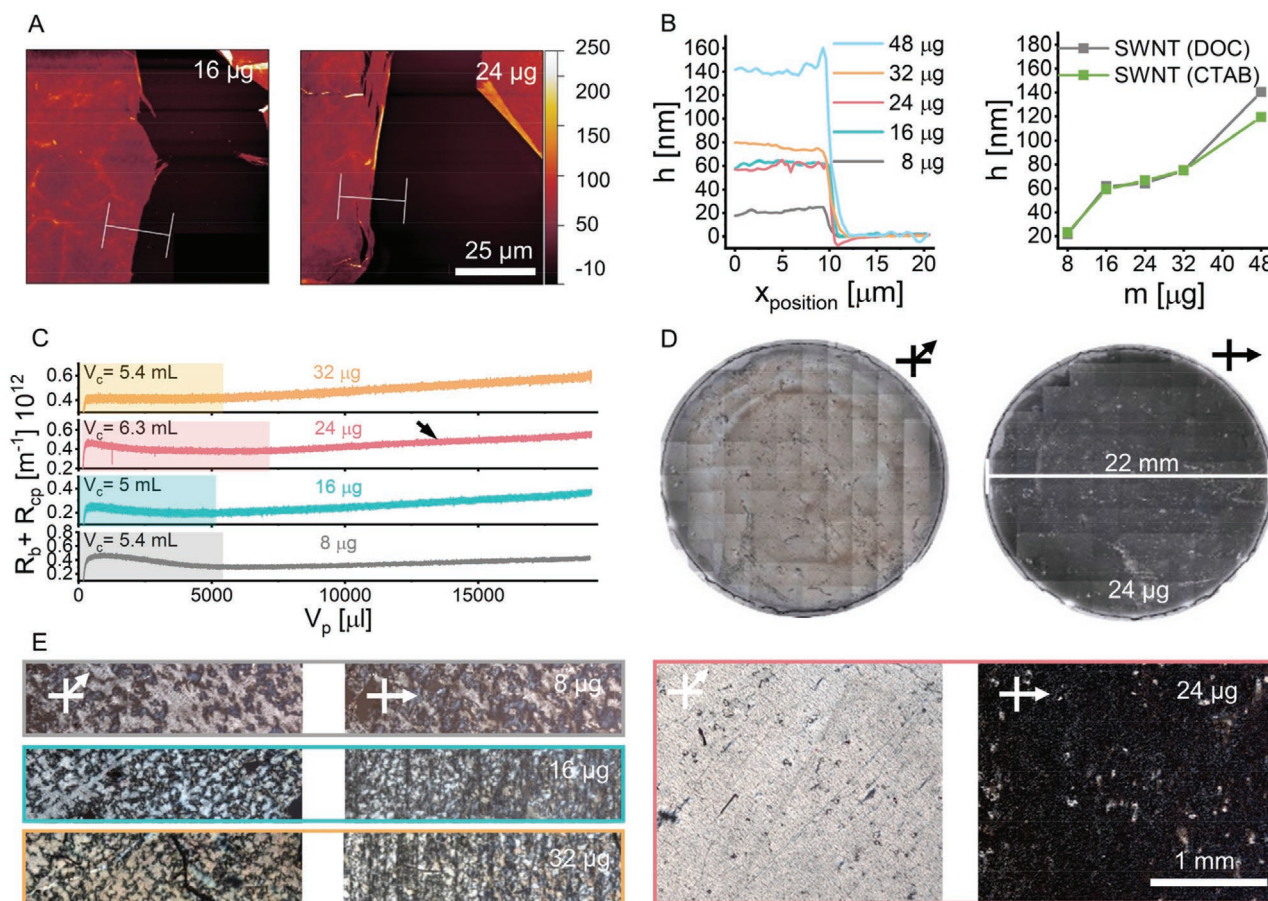


**Figure 4.** A) AFM topography images of SWCNT films transferred to silicon obtained from  $100 \mu\text{L min}^{-1}$  filtration of 2 mL and 3 mL of an  $8 \mu\text{g mL}^{-1}$  dispersion of EA-SWCNTs with 0.04 wt % DOC on an 80 nm membrane. B) Height profile data for feed volumes of 1–6 mL. C) Resistance measured during filtration of 20 mL of a  $0.4\text{--}1.6 \mu\text{g mL}^{-1}$  dispersion of EA-SWCNTs with 0.002–0.016 wt % DOC at volume rate of  $100 \mu\text{L min}^{-1}$  and with push step of  $500 \mu\text{L min}^{-1}$  on an 80 nm membrane. The total mass of SWCNTs filtered was 8–32  $\mu\text{g}$  and the transition between intermediate blocking and cake filtration for the 24  $\mu\text{g}$  case is indicated by an arrow. D) Stitched cross-polarized microscopy images of the film obtained from 24  $\mu\text{g}$  of SWCNTs on the membrane (top surface). E) Cross-polarized microscopy of films after transfer to ITO-coated glass substrates (bottom surface) for SWCNT masses of 8–32  $\mu\text{g}$ .

coated. All other masses displayed only cake filtration and had a similar critical volume of  $\approx 5.25$  mL. Upon stitching 155 individual cross-polarized micrographs taken with  $5\times$  magnification, the  $24\ \mu\text{g}$  sample was found to afford a dense and globally aligned SWCNT film across the entire membrane, Figure 4D. Cross-polarized microscopy of the film after transfer to ITO, Figure 4E and SEM images in Figure S23 (Supporting Information), showed that alignment was consistent on both sides of the film. Here it is important to note that the elongated SWCNT domains seen in Figure S14 (Supporting Information) were still present but that these now had a common alignment direction. In contrast, the other concentrations were found to result in the formation of either an incomplete layer ( $8$  and  $16\ \mu\text{g}$ ) or an overgrown layer ( $32\ \mu\text{g}$ ), Figure 4E. A similar effect was observed for the non-diluted samples use for topography measurements discussed previously, Figure S24 (Supporting Information). The dependence on mass can be understood in

terms of the required mass to fill the membrane homogeneously and further corroborates that the global alignment mechanism involves the formation of crystallites rather than individual SWCNTs.

Having identified precise conditions for global alignment on unmodified membranes, we investigated intentional surface texturing using the hot embossing method.<sup>[44,45]</sup> This was achieved with a custom-made shim containing four different regions with groove spacings of  $w = 150, 300, 450,$  and  $600$  nm, Figure 5A. A hot embossing setup was built from a repurposed tensile test machine, modified with a heating module, and used to imprint these structures into  $80$  nm membranes.<sup>[60]</sup> Hot embossing was performed at a temperature of  $\approx 120\ ^\circ\text{C}$ , which is slightly below the glass transition temperature of polycarbonate ( $147\ ^\circ\text{C}$ <sup>[44]</sup>) and allowed for plastic deformation of the membrane. A Teflon piece with the dimensions of the patterned field and a larger Kapton sheet were used to transmit

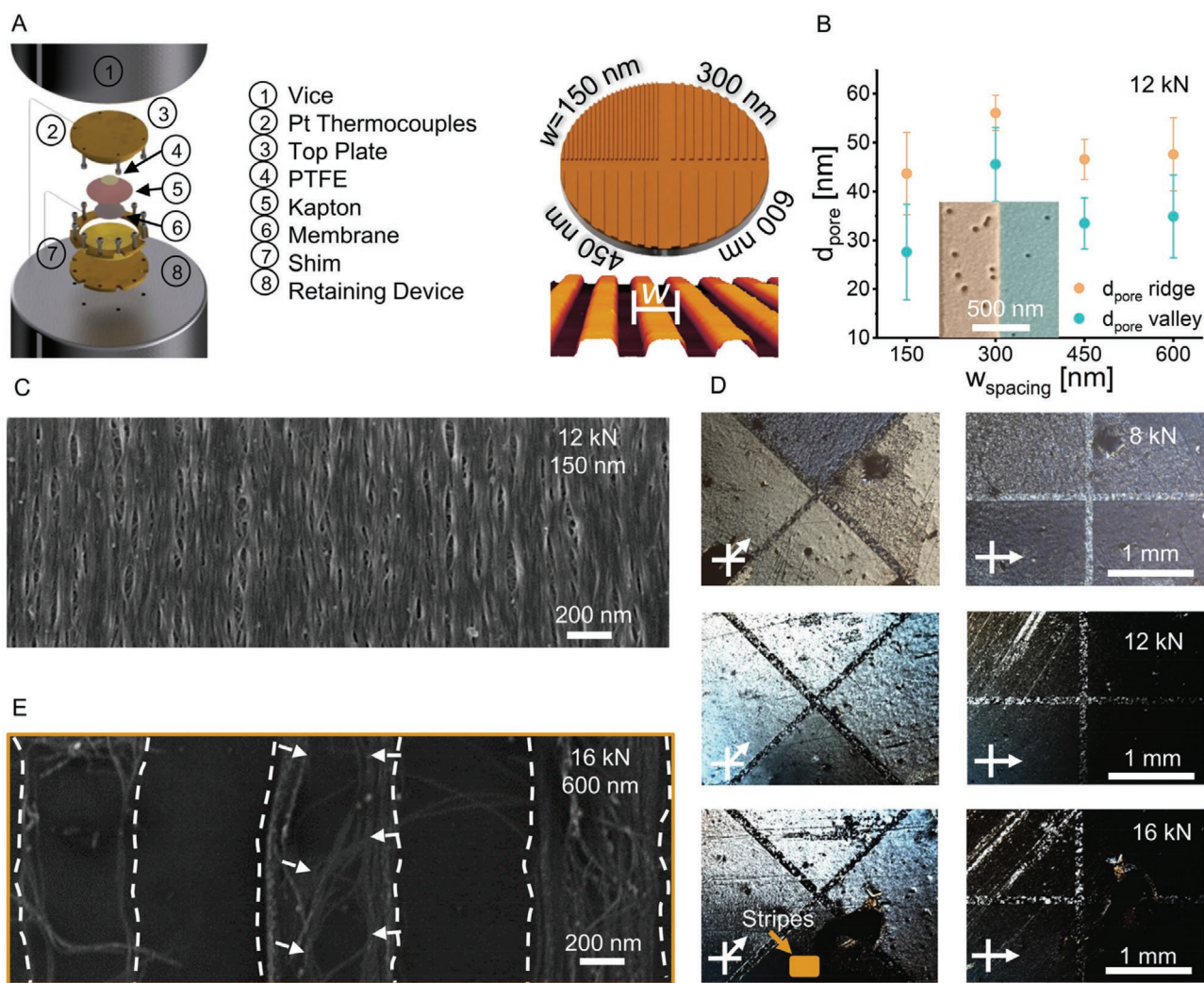


**Figure 5.** A) Schematic of the hot embossing setup and shim used to imprint line spacings of  $150$ – $600$  nm. B) Reduction in the size of the pores on a ridge and in a valley for an  $80$  nm membrane stamped at  $12$  kN. C) SEM image of the SWCNT film obtained by filtration of  $2$  mL of an  $8\ \mu\text{g mL}^{-1}$  EA-SWCNT dispersion in  $0.04$  wt % DOC at  $100\ \mu\text{L min}^{-1}$  with a push step of  $500\ \mu\text{L min}^{-1}$  on  $150$  nm grooves imprinted on an  $80$  nm at  $12$  kN. D) Cross-polarized microscopy images of transferred (silicon-substrate) SWCNT films prepared in the same way but on  $80$  nm membranes imprinted at  $8, 12,$  and  $16$  kN. E) Evolution of SWCNT stripe alignment due to the uneven deformation of pores in valleys and ridges.



and homogenize the force applied. Each pattern had an equivalent cumulative area of grooves and ridges which meant that the smaller lines required greater force for deformation. An applied force of 8 kN was found to be insufficient for the smaller patterns whereas 16 kN deformed the largest pattern. At 12 kN all structures were well replicated in the membrane. AFM images of the textured membranes and further details on the hot embossing process can be found in Figures S25 and S26 in the Supporting Information.

Apart from applying a texture, hot embossing was also accompanied by several other key changes to the membrane. Firstly, greater deformation at the contact area with the shim (valleys) leads to a reduction of the pore size in this region. Figure 5B provides a comparison of the pore size on the ridges and in the valleys for 12 kN of applied force on an 80 nm membrane and the corresponding SEM images can be found in Figure S27 in the Supporting Information. Due to membrane resistance being inversely proportional to the fourth power of the pore diameter this led to an increase in the overall membrane resistance, Figure 2A. Furthermore, a reduction in the absolute zeta potential at the membrane surface from  $-60$  mV for a PVP coated membrane at pH = 8.5 to  $-42$  mV for the hot embossed membrane was observed, Figure 2C.

Intuitively it might be expected that these changes to the membrane would lead to a significant variation in the conditions required for alignment, but in fact, we were able to align SWCNTs on all imprinted membranes, regardless of the mass or volume rate used. Total resistance measurements for the filtration of 2 mL of an  $8 \mu\text{g mL}^{-1}$  EA-SWCNT dispersion in 0.04 wt % DOC at  $100 \mu\text{L min}^{-1}$  and pushed with  $500 \mu\text{L min}^{-1}$  on 80 nm membranes can be found in Figure S25G in the Supporting Information. An SEM image of the resulting SWCNT film for 600 nm grooves is shown in Figure 5C with all groove spacings and applied forces shown in Figure S28 in the Supporting Information. The corresponding cross-polarized microscopy images are shown in Figure 5D. Poor replication of the shim at applied forces of 8 and 16 kN can be seen in regions with less variation in the contrast between bright ( $45^\circ$ ) and dark ( $0^\circ$ ) positions. However, in areas with high deformation it was possible to find regions with incomplete coverage of SWCNTs, such as the 600 nm line spacing imprinted at 16 kN, Figure 5E. It can be seen that SWCNTs first align along the edge of a pattern and then those SWCNTs arriving later align to these until a ridge is fully covered. Contrary to an un-stamped membrane this alignment process now involves the assembly of individual SWCNTs.

Despite their differences, experiments with DOC or CTAB and with or without membrane texturing are similar and can all be understood with a common model. For any flux ( $J$ ) with concentration ( $c$ ), the concentration gradient ( $\frac{dc}{dz}$ ) building up at the membrane surface establishes a diffusive transport component that is in opposition to the convective component ( $J \cdot c$ ) toward the membrane. Additionally, an interaction potential ( $\Phi_{\text{TOT}}$ ) between the surface of the membrane and the filtered species contributes to the flux. This component can either be away from or toward the membrane surface and depends on whether or not the interaction is repulsive or attractive. The net

mass flux ( $N$ ) toward the membrane surface is thus described by the following equation<sup>[61]</sup>

$$N = Jc - D \frac{dc}{dz} - \frac{D}{k_b T} c \frac{d\Phi_{\text{TOT}}}{dz} \quad (3)$$

Using this equation, it can be seen that if the convective transport toward the membrane is counteracted by diffusion and the interaction potential, the particle will remain in a dispersed state, otherwise it will deposit onto the membrane surface. In our work, it was found that alignment was enhanced by diluting the feed solution, which implies that there is a close to homogenous distribution of SWCNTs and a negligible concentration gradient. Therefore, at room temperature the filtration of SWCNTs depends primarily upon the flux,  $J$ , and the interaction potential,  $\Phi_{\text{TOT}}$ . Given that the zeta potential of the membrane and the SWCNTs have been measured, DLVO theory can be used to describe the interaction potential for an isolated SWCNT at the membrane surface.<sup>[40]</sup> Further details on the DLVO calculations can be found in the Supporting Information. The pH of the EA-SWCNT dispersions was 8.5 for DOC and 8.7 for CTAB, Figure 2B, and this implies that during filtration  $\zeta_{\text{surf}}$  assumes a value of  $\approx -42$  mV for the hot embossed (HE) membranes,  $-60$  mV for the PVP-coated (PVP) membranes and  $-110$  mV for the uncoated (UC) membranes.  $\Phi_{\text{TOT}}$  was calculated as the sum of the electrical double layer ( $\Phi_{\text{EDL}}$ ) and van der Waals ( $\Phi_{\text{VDW}}$ ) interactions at a distance  $z$ , above the membrane surface. Ideally,  $\Phi_{\text{EDL}}$  requires knowledge of the surface potential ( $\gamma$ ) of the SWCNTs and the membrane, but these were approximated from their zeta potentials using the approach of Wu et al.<sup>[40]</sup> In the case of DOC dispersed SWCNTs, the membrane and the SWCNTs have a zeta potential of equal sign and this leads to an  $\Phi_{\text{EDL}}$  that is repulsive whilst for CTAB dispersed SWCNTs they have opposite sign and  $\Phi_{\text{EDL}}$  is attractive. In both cases  $\Phi_{\text{VDW}}$  is always attractive. These two cases are shown in Figure S29 in the Supporting Information. For DOC dispersed SWCNTs,  $\Phi_{\text{TOT}}$  has a shallow secondary minimum located 23.7 nm (HE), 25 nm (PVP), or 26.4 nm (UC) above the membrane surface, while the primary minimum is found on the surface itself. Figure 6A displays  $\Phi_{\text{TOT}}$  for membrane potentials ranging from  $-120$  to  $-10$  mV, where it can be seen that the location of the minimum approaches the surface for less negative zeta potentials. Due to the absence of a repulsive component in the case of CTAB, there is no secondary minimum and the SWCNTs are attracted directly to the surface, Figure 6B.

We found that an increase in filtration resistance was essential for the alignment of SWCNTs regardless of the dispersions or membranes used. This indicates that the SWCNTs must accumulate on the membrane surface and not within the secondary minimum as suggested by others in the field.<sup>[27,39,43,44,46]</sup> For DOC dispersed SWCNTs, this requires the SWCNTs to overcome the potential barrier to the surface utilizing the applied convective flux, as illustrated in Figure 6C. On the contrary, SWCNTs which are not reaching the surface will lead to concentration polarization and gather behind the potential barrier, which occurs at low volume rates ( $25\text{--}75 \mu\text{L min}^{-1}$ ). The optimum volume rate ( $100 \mu\text{L min}^{-1}$ ) overcomes the potential barrier, minimizes concentration polarization and



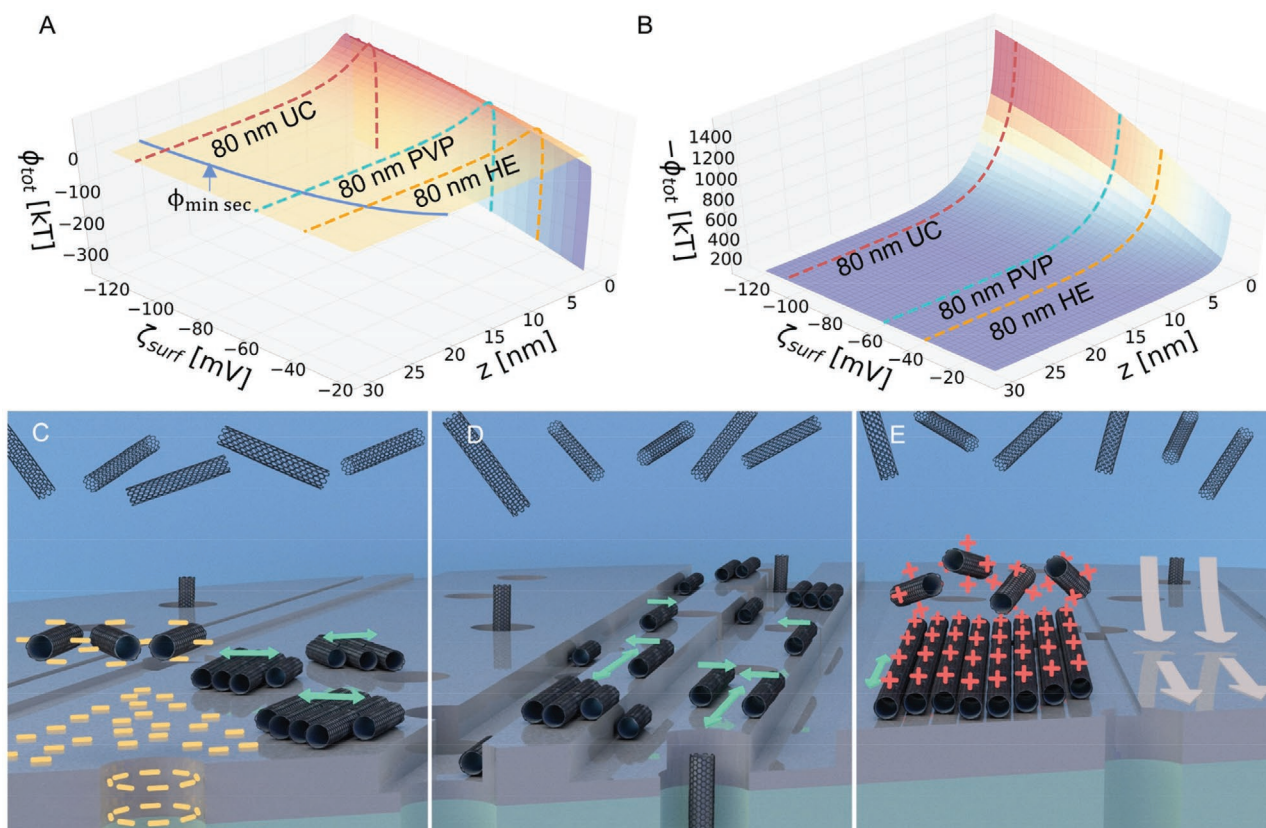


**Figure 6.** Calculation of the total potential  $\Phi_{TOT}(z)$  of a A) DOC and B) CTAB dispersed SWCNT with respect to the zeta potential of the membrane surface  $\zeta_{surf}$  utilizing DLVO theory.<sup>[40]</sup> The potential corresponding to an uncoated (UC), PVP coated and hot embossed (HE) 80 nm membrane are marked with a dashed line, as well as the shallow secondary minimum ( $\approx -0.15$  kT). Illustration of the alignment of C) DOC dispersed SWCNTs on a pristine PVP coated membrane, D) a hot embossed membrane and E) CTAB dispersed SWCNTs on an untextured membrane. The beige arrows indicate shear flow parallel to the membrane which acts as an alignment director for the SWCNTs.

allows SWCNT crystallites to grow on the membrane surface. At higher volume rates ( $125 \mu\text{L min}^{-1}$ ), we propose that turbulence disturbs these crystallites and once again a disordered layer and an increase in the concentration polarization volume is obtained. In the case that the membrane is textured (Figure 6D), a lower surface zeta potential ( $-49$  mV) results in the secondary minimum being slightly closer to the surface (23.7 nm) but more importantly, at a distance that is shorter than the depth of the grooves (80 nm). This means that a CNT approaching the surface can circumvent the potential barrier at the edge of a groove because of a discontinuity in its position from the surface at this edge, Figure S30 in the Supporting Information. This leads to the observation of almost no concentration polarization regime in Figure S25G in the Supporting Information and allows for the SWCNTs to assemble immediately on the membrane surface. Due to the fact that these initial CNTs are all orientated in the same direction no grain boundaries and thus crystallites are observed. For CTAB, the SWCNTs also accumulate directly on the surface regardless of the volume rate applied, Figure 6E. However, unlike in the case of DOC, the concentration of SWCNTs within this initial fouling step ( $500 \mu\text{L}$ ) is not sufficient to form crystallites and the high surface charge on the CTAB dispersed SWCNTs ( $\zeta_{CTAB} = +72$  mV versus  $\zeta_{DOC} = -14$  mV) results in the first

layer of SWCNTs establishing a new potential barrier and a secondary minimum to the surface. This is evidenced by the secondary concentration polarization regime seen in Figure S16 in the Supporting Information.

For textured surfaces the driving force for global alignment can easily be understood. A pore size difference between the ridges and valleys provides a directional flow through the ridges and this is combined with a negligible potential barrier at the edges. This drives the SWCNTs to first assemble at the edges and follow the embossed pattern, Figure 5E. However, the driving force for alignment on un-textured membranes appears to be more complex. Both positive and negatively charged SWCNTs were found to align and pre-existing grooves in the membrane appeared to be less important, Figure 3D. Clearly there must be an additional interaction between the membrane and SWCNTs in order to drive global alignment. Due to the proven close proximity of the SWCNTs to the membrane surface and the elongation of the crystallites with increasing volume rate we speculate that shear flow across the membrane surface is responsible for alignment. Due to the 1D structure of the CNTs, this flow needs to be either uni- or bi-directional and it is intuitively difficult to understand where such a shear flow should originate for a dead-end filtration setup on a symmetric and circular membrane. Here we speculate that the

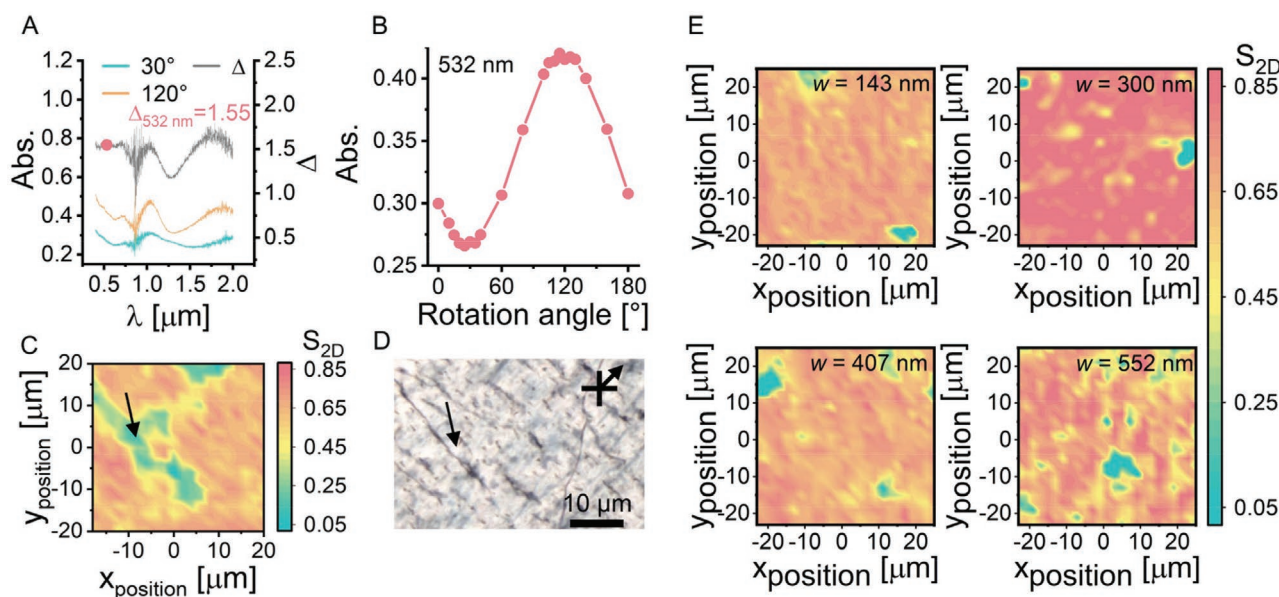


**Figure 7.** A) Measurement of the dichroic ratio of the sample shown in Figure 4E. B) Angular dependence of the absorbance at 532 nm used to generate the Raman maps. C)  $S_{2D}$  map of globally aligned film on an untextured membrane and D) the corresponding cross-polarized light microscopy image in the bright position ( $45^\circ$ ) of a transferred film (silicon substrate). The black arrow indicates the position of a grain boundary. E)  $S_{2D}$  maps of films on a 12 kN hot embossed membrane shown in Figure 5D at various groove spacing.

average direction of grooves present in the membrane from manufacture provide a directionality to the flow of liquid across the surface and that these drive the alignment of CNTs. In this way, it is possible for certain isolated grooves to be misaligned with the overall direction of all others and hence the liquid flow across the surface. This will lead to the observation that occasionally, and in localized regions, that CNTs and grooves can be misaligned.

The extent of alignment for each case was evaluated by the  $S_{2D}$  parameter using Raman spectroscopy and the approach of Zamora-Ledezma et al.<sup>[17c,46]</sup> This requires precise knowledge of the dichroic ratio ( $\Delta$ ), which was obtained from absorption spectra (400–2400 nm) of the aligned film shown in Figure 5E,F measured at intervals of  $15^\circ$  with linear polarized light, Figure 7A. Close to the absorption minima and maxima, finer intervals of  $1^\circ$  were used and the maximum was divided by the minimum to obtain the dichroic ratio, Figure 7B. As expected, the positions of the maximum and minimum were offset by  $90^\circ$  to each other. Our Raman measurements were conducted with a laser wavelength of 532 nm and a dichroic ratio of  $\Delta_{UV\ 532nm} = 1.55$ , see experimental methods. The dichroic ratio was additionally measured with an optical power meter and a polarizer in our Raman setup and this afforded a value of  $\Delta_{PM\ 532nm} = 1.52$ . The additional Raman intensities ( $I_{HH}$ ,  $I_{HV}$ ,  $I_{VV}$  and  $I_{VH}$ ) are shown in Figure S31 in the Supporting Information and these allowed for 2D Raman maps ( $1520\ \mu m^2$ ) of the  $S_{2D}$  parameter to be generated. For the un-textured surfaces, the disordered grain boundaries are clearly visible as regions of low  $S_{2D}$ , Figure 7C. For comparison, a cross-polarized microscopy image of a grain boundary on the same film is shown in Figure 7D. For the textured surfaces a more uniform  $S_{2D}$  map was obtained and without the presence of grains. The small misaligned regions are a result of poor shim replication as seen by AFM

in Figure S26 in the Supporting Information. We found the highest alignment ( $S_{2D} = 0.85$ ) on a spacing of 300 nm. Interestingly the 150 nm grooves did not show a further increase in alignment. We speculate that this is because the groove depth ( $\approx 4.5$  nm), Figure S25D in the Supporting Information, was well below the distance of the secondary potential minimum (23.7 nm), whereas the 300 nm membrane had a groove height of  $\approx 178$  nm. Additionally, the optimal width of a groove might depend on the length and diameter of the SWCNT's, due to a change in van der Waals forces between the nanotubes and the resulting size of bundles depending on those forces.

### 3. Conclusion

Spontaneous global alignment of carbon nanotubes using dead-end filtration was achieved on textured and un-textured membranes and with positively and negatively charged surfactants. In the case of a slightly negatively charged surfactant (DOC) with a PVP coated membrane, the repulsion of the nanotubes by the electric double layer potential has to be overcome in order to grow SWCNT crystallites on the surface of the membrane. Crystallites were found to align in a direction not always coinciding with the grooves present in the membrane and a rapid transition from concentration polarization to a fouling regime was required. The volume rate at the beginning of filtration was found to be most important and a resolution of at least  $\pm 25\ \mu L\ min^{-1}$  is required. Additionally, a filtered mass of  $24\ \mu g$  for a membrane area of  $3.8\ cm^2$  and a nanotube concentration of  $1.6\ \mu g\ mL^{-1}$  was found to facilitate the best alignment. The final pushing and drying steps were found to have little effect on the overall alignment. Alternatively, hot embossing of the membrane was found to reduce the surface zeta potential

and more importantly create edge sites at which the surface potential barrier was negligible. This prevented the formation of grains or a concentration polarization regime and enabled the SWCNTs to adhere directly to the membrane. Here, the role of the filtered mass and the volume rate were found to be less important. In the case of a positively charged surfactant (CTAB) on a PVP coated membrane a disordered layer was found to be sandwiched between two highly aligned layers. This was a consequence of highly charge nanotubes in the first aligned layer establishing an intermediate concentration polarization regime. Here, the formation of grains was also not found to be a requirement for global alignment. This indicates that the director for global alignment for an un-textured membrane is not related to the electric double layer as suggested by other researchers. In fact, electronic repulsion leads to the formation of domains and a less aligned film due to the presence of grain boundaries. In this system, the charge on nanotubes can be better understood as a parameter that must be overcome in order to bring the nanotubes into close proximity with each other and/or the membrane surface. In this regard, the difficulty to align small diameter and/or short carbon nanotubes with this method likely stems from a reduction in van der Waals potential that places the nanotubes further from the membrane surface and inhibits their agglomeration.

#### 4. Experimental Section

**Suspensions of SWCNTs:** Following previously reported protocols,<sup>[62]</sup> 40 mg of EA-P2 (lot no. 02-A011, Carbon Solutions) SWCNTs were dispersed in a 40 mL aqueous solution of either 2 % sodium deoxycholate (DOC) (20 gL<sup>-1</sup>, BioXtra 98+%) or 0.5 % CTAB (5 gL<sup>-1</sup>, Sigma-Aldrich) by tip sonication for 45 min (0.9 WmL<sup>-1</sup>) in an ice bath followed by centrifugation (45,560g, Beckman Optima L-80 XP, SW 40 Ti rotor) for 1 h. The top eighty percent of the supernatant was collected and used further. All dispersions were prepared with deionized water (18.2 MΩcm, pH = 6.93) from an Arium pro UV (Sartorius).

**Membranes:** All membranes were obtained from it4ip with a diameter of 47 mm, a pore density of  $6 \times 10^8$  cm<sup>-2</sup> and a thickness of 25 μm.

**Spectroscopy:** UV–VIS–NIR absorbance spectra of nanotube dispersions were collected on a Cary 500 spectrometer from 1880 to 200 nm in 1 nm increments through a 1 mm glass cuvette. The dichroic ratio was determined with a Lambda 1050 spectrometer (Perkin Elmer) with an integrating sphere module, 2 mm beam spot, and Glan-Thompson polarizing prism. Raman experiments were conducted with a Horiba Xplora spectrometer, equipped with a 2.33 eV laser source. The laser was focused on the aligned nanotubes with a 100× (0.95 N.A.) objective. The laser power was 100 μW. The backscattered light was collected with the same objective, dispersed by 1200 grooves per mm grating and detected by a Silicon charge coupled device. A built-in half wave plate was used to rotate the laser polarization perpendicular or parallel to the alignment direction. In a similar manner the analyzer was set for the desired direction. For the orientation parameter  $S_{2D}$  calculation in two dimensions, following equation was used<sup>[17c]</sup>

$$S_{2D} = \frac{\Delta I_{VV} - I_{HH}}{\Delta I_{VV} + I_{HH} + (1 + \Delta) I_{VH}} \quad (4)$$

where  $I_{XY}$  indicates the G mode intensity (integrated area of the peak) with the incident light polarized along X and analyser oriented toward Y. X and Y can take either V or H values, parallel or perpendicular to the orientation of the SWCNTs inside the film respectively.  $\Delta_{UV, 532nm}$  is the optical dichroic ratio at 532 nm, measured to be 1.55. We measured  $I_{HH}$ ,  $I_{VV}$ , and  $I_{VH}$  at every of the lateral position in a 24 × 24 μm map, with 2 μm sampling. The

different sensitivity in the vertical and horizontal directions was calibrated by Raman signals from Benzonitrile molecules. For polarization rotation experiments, the home built half wave plate was introduced into the incident and scattered paths of the light. The intensity was collected for a series of incident angles (~5° steps). The fit is provided by a standard equation for this phonon, where intensity varies as

$$I(\alpha) = I_{\parallel} \cos(\alpha)^4 I_{\perp} \quad (5)$$

**Scanning Electron Microscopy:** Images were taken with a Zeiss Ultra Plus with a 30 μm aperture and an acceleration voltage of 2 kV.

**Light Microscopy and Cross-Polarized Microscopy:** A Leica DMLM light microscope was used to capture images of the drying rings and make cross-polarized measurements of membrane and substrate supported films. Cross-polarized images were obtained in reflectance with two linear polarizers. Incident light was polarized by 90° with respect to the analyzer. To record the images for dark (0°) and bright position (45°), a rotational stage was placed on the microscope table and rotated to identify the position with maximum intensity. All images are recorded with the same brightness and exposure time. Images were analyzed with ImageJ and the open-source extension shape logic was used to determine the area of the individual grains.

**AFM Microscopy:** Topographies were recorded with a Dimension Icon, Bruker with NSC 19 cantilevers (μmasch) with a resonance frequency of 65 kHz and a force constant of 0.5 N m<sup>-1</sup>. Imaging was performed in the repulsive regime with standard tapping mode in air and a resolution of 1024 lines. All topographies were evaluated using open-source Gwyddion. For the length determination, 30 μL of ten times diluted dispersion were spin coated onto a silicon wafer at 2000 rpm for 3 min.

**Zeta Potential of the Membranes:** All measurements were performed with a Surpass, Anton Paar. The pH and conductivity probes were calibrated with buffer solutions (pH 4,7 and 10) and a KCl standard, respectively. The surface zeta potential was measured in a gap cell with a height adjusted to 100 μm. The pH tested was increased in steps of 0.5 from pH 4 to pH 10 and three successive zeta potentials were measured and averaged at each value. The pore zeta potential was measured in a similar fashion, albeit with a cylindrical cell and with the membrane cut to a diameter of 13 mm.

**Zeta Potential of SWCNT Dispersions:** Solution zeta potentials were measured with a Zetasizer Nano ZS, Malvern. The Smoluchowski model was used to evaluate the zeta potential from the hydrodynamic radius calculated from the auto correlation function and the electrophoretic mobility using the integrated PALS system, with the constants of pure water at 25 °C ( $\nu = 0.8872$  mm<sup>2</sup> s<sup>-1</sup>,  $n = 1.33$  and  $\epsilon_r = 78.5$ ).

**Film Transfer:** SWCNT films were transferred either to ITO glass substrates (PGO,  $20 \pm 6$  Ωm<sup>-1</sup>, and  $1.0 \pm 0.1$  mm thickness) or Si wafers (CrysTec, polished and etched, thickness 525 μm, p-type, specific resistance > 1 Ωcm) using the method outlined by Walker et al.<sup>[46]</sup> Membranes were dissolved with Chloroform (99.2 % stabilized with 0.6 % ethanol, VWR chemicals) and adhered to the surface at 50 °C.

**DLVO Calculation:** DLVO Plots were realized with the Anaconda 3 jupyter notebook using python 3 with numpy and scipy packages. The original derivation is described by Wu et al.<sup>[40]</sup>

**Shim Production:** The pattern of the shim has been programmed with Klayuter, Open Source and converted into a machine readable format by LayoutBEAMER Software from GenSYS. Following a substrate baking step (180 °C for 300 s) a PMMA resist (AR-P 672.045; Allresist GmbH), spin-coated at 3000 rpm for 60 s onto a non-oxidized standard silicon wafer to a height of 100 nm was used for electron beam lithography. An optimal dose of 380 μC cm<sup>-2</sup> yielded the best structure quality. After exposure, the nanostructures in PMMA were developed in a solution of methyl isobutyl ketone (MIBK) and isopropyl alcohol (IPA) in a concentration ratio 1:3 by spray development. Chromium (7 nm) and gold (25–30 nm) layers were evaporated on top of the wafer and PMMA structures. The chromium layer serves as adhesive layer and the gold layer as conductive plating base for the subsequent deposition of nickel. During metallization the substrate was tilted at 30°. For the nickel deposition the metallized nanostructured wafer was immersed in an electrolytic bath. Electroplating was carried out in a boric acid containing



nickel sulphamate electrolyte (pH 3.4 to 3.6 at 52 °C) for 43 h. To ensure a slow growth of the nickel layer and to achieve a defect-free filling of the irradiated nanostructured areas the current density was adjusted to 0.25 A dm<sup>-2</sup> (corresponding a growth speed of approximately 0.05 μm min<sup>-1</sup>) at the beginning of the plating process. After 30 minutes the current density was increased to 0.5 A dm<sup>-2</sup> (approx. 0.1 μm min<sup>-1</sup>) and in further steps up to 1.0 A dm<sup>-2</sup> (approx. 0.2 μm min<sup>-1</sup>). A shim thickness of at least 500 μm was required. The nickel shim was separated using a simple lift-off process and subsequently the resist was stripped with acetone (60 s) and the shim cleaned with IPA (60 s, shaker). Metallization layers (gold and chromium) were not etched and remain on the surface of the nickel shim.

**Filtration:** The custom filtration setup was built from microfluidic components obtained from Elveflow. This is included the regulator (OB1 MK3+), pressure sensors (MPS1 and MPS2), Coriolis flow sensor (BFS1+) and bubble trap (44 μL). Line switching was realized by two 3/2 solenoid Whisper valves (type 6724) from Bürkert, operated at 24 V and controlled by a custom-built Arduino UNO. The filtration cell was realized by an in-house workshop and made of stainless steel and PTFE cylinders. The sieve consists of two stainless steel metal sheets fixing a 280 μm mesh (Fteu). A G2258A UV diode array (Agilent) was used for in situ absorption measurements. In order to prevent contamination, bottled nitrogen with a purity of 99.999 % and air filters prior to the regulator was used. The gas line tubing (red) consisted solely of 1/8" PTFE tubing with an inner diameter of 1.6 mm. The fluid lines (blue) were 1/16" PTFE tubing with an inner diameter of 1 mm, except for the lines connecting the Coriolis flow sensor, which employ Swage Lock® fittings and require stiffer PEEK tubing. All capillaries were purchased from Techlab. The program code was written with Labview (National Instruments) utilizing software packages from Elveflow and open-source LyNx for the Arduino.

## Supporting Information

Supporting Information is available from the Wiley Online Library or from the author.

## Acknowledgements

B.S.F., C.R., and H.L. gratefully acknowledge support from the Deutsche Forschungsgemeinschaft (DFG) under grant numbers FL 834/2-1, FL 834/2-2, FL 834/5-1, and FL 834/7-1. C.R. thanks Marc Schneider for assistance with hot embossing. This work was partly carried out with the support of the Karlsruhe Nano Micro Facility, a Helmholtz Research Infrastructure at Karlsruhe Institute of Technology.

Open access funding enabled and organized by Projekt DEAL.

## Conflict of Interest

The authors declare no conflict of interest.

## Data Availability Statement

Research data are not shared.

## Keywords

1D crystals, aligned nanomaterials, membranes, polarizers, thin films, zeta potential

Received: July 29, 2021

Revised: October 19, 2021

Published online:

- [1] a) M. S. Dresselhaus, G. Dresselhaus, P. Avouris, *Carbon Nanotubes: Synthesis, Structure, Properties and Applications*, Springer, Berlin **2001**; b) A. Jorio, G. Dresselhaus, M. S. Dresselhaus, *Carbon Nanotubes: Advanced Topics in the Synthesis, Structure, Properties and Applications*, Springer, Berlin **2008**; c) R. Saito, G. Dresselhaus, M. S. Dresselhaus, *Physical Properties of Carbon Nanotubes*, Imperial College, London **1998**; d) M. Pfohl, D. D. Tune, A. Graf, J. Zaumseil, R. Krupke, B. S. Flavel, *ACS Omega* **2017**, *2*, 1163.
- [2] a) M. S. Dresselhaus, G. Dresselhaus, R. Saito, *Carbon* **1995**, *33*, 883; b) M. S. Arnold, J. L. Blackburn, J. J. Crochet, S. K. Doorn, J. G. Duque, A. Mohite, H. Telg, *Phys. Chem. Chem. Phys.* **2013**, *15*, 14896; c) T. W. Ebbesen, P. M. Ajayan, *Nature* **1992**, *358*, 220.
- [3] a) M. Pfohl, K. Glaser, J. Ludwig, D. D. Tune, S. Dehm, C. Kayser, A. Colsmann, R. Krupke, B. S. Flavel, *Adv. Energy Mater.* **2016**, *6*, 1501345; b) M. Pfohl, K. Glaser, A. Graf, A. Mertens, D. D. Tune, T. Puerckhauer, A. Alam, L. Wei, Y. Chen, J. Zaumseil, A. Colsmann, R. Krupke, B. S. Flavel, *Adv. Energy Mater.* **2016**, *6*, 1600890; c) B. J. Landi, M. J. Ganter, C. D. Cress, R. A. DiLeo, R. P. Raffaele, *Energy Environ. Sci.* **2009**, *2*, 638; d) A. Varga, M. Pfohl, N. A. Brunelli, M. Schreier, K. P. Giapis, S. M. Haile, *Phys. Chem. Chem. Phys.* **2013**, *15*, 15470; e) D. D. Tune, B. S. Flavel, *Adv. Energy Mater.* **2018**, *8*, 1703241; f) L. Wieland, H. Li, C. Rust, J. H. Chen, B. S. Flavel, *Adv. Energy Mater.* **2021**, *11*, 2002880; g) J. L. Blackburn, *ACS Energy Lett.* **2017**, *2*, 1598; h) A. Classen, L. Einsiedler, T. Heumueller, A. Graf, M. Brohmann, F. Berger, S. Kahmann, M. Richter, G. J. Matt, K. Forberich, J. Zaumseil, C. J. Brabec, *Adv. Energy Mater.* **2018**, *8*, 1801913; i) M. Gong, T. A. Shastry, Q. Cui, R. R. Kohlmeier, K. A. Luck, A. Rowberg, T. J. Marks, M. F. Durstock, H. Zhao, M. C. Hersam, S. Ren, *ACS Appl. Mater. Interfaces* **2015**, *7*, 7428.
- [4] a) P. Avouris, M. Freitag, V. Perebeinos, *Nat. Photonics* **2008**, *2*, 341; b) F. Pyatkov, V. Fütterling, S. Khasminskaya, B. S. Flavel, F. Hennrich, M. M. Kappes, R. Krupke, W. H. P. Pernice, *Nat. Photonics* **2016**, *10*, 420; c) M. Engel, K. E. Moore, A. Alam, S. Dehm, R. Krupke, B. S. Flavel, *ACS Nano* **2014**, *8*, 9324.
- [5] a) B. S. Flavel, J. Yu, J. G. Shapter, J. S. Quinton, *J. Mater. Chem.* **2007**, *17*, 4757; b) M. Steiner, M. Engel, Y.-M. Lin, Y. Wu, K. Jenkins, D. B. Farmer, J. J. Humes, N. L. Yoder, J.-W. T. Seo, A. A. Green, M. C. Hersam, R. Krupke, P. Avouris, *Appl. Phys. Lett.* **2012**, *101*, 053123.
- [6] a) X. Yu, B. Munge, V. Patel, G. Jensen, A. Bhirde, J. D. Gong, S. N. Kim, J. Gillespie, J. S. Gutkind, F. Papadimitrakopoulos, J. F. Rusling, *J. Am. Chem. Soc.* **2006**, *128*, 11199; b) M. Pfohl, K. Glaser, J. Ludwig, D. D. Tune, S. Dehm, C. Kayser, A. Colsmann, R. Krupke, B. S. Flavel, *Adv. Energy Mater.* **2016**, *6*, 1600890; c) D. D. Tune, F. Hennrich, S. Dehm, M. F. G. Klein, K. Glaser, A. Colsmann, J. G. Shapter, U. Lemmer, M. M. Kappes, R. Krupke, B. S. Flavel, *Adv. Energy Mater.* **2013**, *3*, 1091; d) D. J. Bindl, N. S. Safron, M. S. Arnold, *ACS Nano* **2010**, *4*, 5657.
- [7] a) H. B. Hu, S. C. Wang, X. L. Feng, M. Pauly, G. Decher, Y. Long, *Chem. Soc. Rev.* **2020**, *49*, 509; b) B. Su, Y. C. Wu, L. Jiang, *Chem. Soc. Rev.* **2012**, *41*, 7832.
- [8] R. Saito, M. S. Ukhary, S. K. Wang, Y. Iwasaki, *J. Appl. Phys.* **2020**, *128*, 164301.
- [9] a) A. Baydin, N. Komatsu, F. Tay, S. Ghosh, T. Makihara, G. T. Noy, J. Kono, *Optica* **2021**, *8*, 760; b) L. Ren, C. L. Pint, L. G. Booshehri, W. D. Rice, X. Wang, D. J. Hilton, K. Takeya, I. Kawayama, M. Tonouchi, R. H. Hauge, J. Kono, *Nano Lett.* **2009**, *9*, 2610.
- [10] Z. Li, K. R. Jinkins, D. Cui, M. Chen, Z. Zhao, M. S. Arnold, C. Zhou, *Nano Res.* **2021**, <https://doi.org/10.1007/s12274-021-3567-9>.
- [11] a) D. D. Tune, B. W. Stolz, M. Pfohl, B. S. Flavel, *Nanoscale* **2016**, *8*, 3232; b) D. Wang, P. C. Song, C. H. Liu, W. Wu, S. S. Fan, *Nanotechnology* **2008**, *19*, 075609.
- [12] a) S. J. Kang, C. Kocabas, T. Ozel, M. Shim, N. Pimparkar, M. A. Alam, S. V. Rotkin, J. A. Rogers, *Nat. Nanotechnol.* **2007**, *2*,

- 230; b) A. Ismach, D. Kantorovich, E. Joselevich, *J. Am. Chem. Soc.* **2005**, *127*, 11554.
- [13] a) G. Giancane, A. Ruland, V. Sgobba, D. Manno, A. Serra, G. M. Farinola, O. H. Omar, D. M. Guldi, L. Valli, *Adv. Funct. Mater.* **2010**, *20*, 2481; b) Q. Cao, S. J. Han, G. S. Tulevski, Y. Zhu, D. D. Lu, W. Haensch, *Nat. Nanotechnol.* **2013**, *8*, 180.
- [14] a) H. Li, T. C. Hain, A. Muzha, F. Schoppler, T. Hertel, *ACS Nano* **2014**, *8*, 6417; b) M. Engel, J. P. Small, M. Steiner, M. Freitag, A. A. Green, M. C. Hersam, P. Avouris, *ACS Nano* **2008**, *2*, 2445; c) G. J. Brady, Y. Joo, S. S. Roy, P. Gopalan, M. A. Arnold, *Appl. Phys. Lett.* **2014**, *104*, 083107; d) Y. Joo, G. J. Brady, C. Kanimozhi, J. Ko, M. J. Shea, M. T. Strand, M. S. Arnold, P. Gopalan, *ACS Appl. Mater. Interfaces* **2017**, *9*, 28859.
- [15] a) M. D. Lynch, D. L. Patrick, *Nano Lett.* **2002**, *2*, 1197; b) R. Krupke, F. Hennrich, H. von Lohneysen, M. M. Kappes, *Science* **2003**, *301*, 344.
- [16] L. Jin, C. Bower, O. Zhou, *Appl. Phys. Lett.* **1998**, *73*, 1197.
- [17] a) X. Li, Y. Jung, K. Sakimoto, T.-H. Goh, M. A. Reed, A. D. Taylor, *Energy Environ. Sci.* **2013**, *6*, 879; b) E. K. Hobbie, D. J. Fry, *Phys. Rev. Lett.* **2006**, *97*, 036101; c) C. Zamora-Ledezma, C. Blanc, M. Maugey, C. Zakri, P. Poulin, E. Anglaret, *Nano Lett.* **2008**, *8*, 4103; d) D. D. Tune, A. J. Blanch, C. J. Shearer, K. E. Moore, M. Pfohl, J. G. Shapter, B. S. Flavel, *ACS Appl. Mater. Interfaces* **2015**, *7*, 25857.
- [18] M. S. Arnold, S. I. Stupp, M. C. Hersam, *Nano Lett.* **2005**, *5*, 713.
- [19] X. Huang, R. S. McLean, M. Zheng, *Anal. Chem.* **2005**, *77*, 6225.
- [20] a) K. E. Moore, M. Pfohl, F. Hennrich, V. S. K. Chakradhanula, C. Kuebel, M. M. Kappes, J. G. Shapter, R. Krupke, B. S. Flavel, *ACS Nano* **2014**, *8*, 6756; b) H. Li, G. Gordeev, S. Wasserroth, V. S. K. Chakradhanula, S. K. C. Neelakandhan, F. Hennrich, A. Jorio, S. Reich, R. Krupke, B. S. Flavel, *Nat. Nanotechnol.* **2017**, *12*, 1176.
- [21] a) M. S. Arnold, A. A. Green, J. F. Hulvat, S. I. Stupp, M. C. Hersam, *Nat. Nanotechnol.* **2006**, *1*, 60; b) H. Gui, J. K. Streit, J. A. Fagan, A. R. H. Walker, C. W. Zhou, M. Zheng, *Nano Lett.* **2015**, *15*, 1642; c) C. Y. Khripin, J. A. Fagan, M. Zheng, *J. Am. Chem. Soc.* **2013**, *135*, 6822.
- [22] a) M. Zheng, A. Jagota, M. S. Strano, A. P. Santos, P. Barone, S. G. Chou, B. A. Diner, M. S. Dresselhaus, R. S. Mclean, G. B. Onoa, *Science* **2003**, *302*, 1545; b) D. Yang, L. Li, X. Wei, Y. Wang, W. Zhou, H. Kataura, S. Xie, H. Liu, *Sci. Adv.* **2021**, *7*, eabe0084; c) H. P. Liu, D. Nishide, T. Tanaka, H. Kataura, *Nat. Commun.* **2011**, *2*, 309; d) H. Li, G. Gordeev, O. Garrity, S. Reich, B. S. Flavel, *ACS Nano* **2019**, *13*, 2567.
- [23] a) X. Wei, T. Tanaka, T. Hirakawa, Y. Yomogida, H. Kataura, *J. Am. Chem. Soc.* **2017**, *139*, 16068; b) H. Li, G. Gordeev, O. Garrity, N. A. Peyyety, P. B. Selvasundaram, S. Dehm, R. Krupke, S. Cambre, W. Wenseleers, S. Reich, M. Zheng, J. A. Fagan, B. S. Flavel, *ACS Nano* **2020**, *14*, 948.
- [24] K. R. Jinkins, J. Chan, R. M. Jacobberger, A. Berson, M. S. Arnold, *Adv. Electron. Mater.* **2019**, *5*, 1800593.
- [25] a) P. Kim, S. Baik, K. Y. Suh, *Small* **2008**, *4*, 92; b) J. Q. Li, Q. Zhang, Y. H. Yan, S. Li, L. Q. Chen, *IEEE Trans. Nanotechnol.* **2007**, *6*, 481.
- [26] a) X. Tu, A. R. Hight Walker, C. Y. Khripin, M. Zheng, *J. Am. Chem. Soc.* **2011**, *133*, 12998; b) F. Yang, M. Wang, D. Q. Zhang, J. Yang, M. Zheng, Y. Li, *Chem. Rev.* **2020**, *120*, 2693; c) D. Janas, *Mater. Chem. Front.* **2018**, *2*, 36.
- [27] X. W. He, W. L. Gao, L. J. Xie, B. Li, Q. Zhang, S. D. Lei, J. M. Robinson, E. H. Haroz, S. K. Doorn, W. P. Wang, R. Vajtai, P. M. Ajayan, W. W. Adams, R. H. Hauge, J. Kono, *Nat. Nanotechnol.* **2016**, *11*, 633.
- [28] P. Bacchin, P. Aimar, R. W. Field, *J. Membr. Sci.* **2006**, *281*, 42.
- [29] a) G. B. van den Berg, C. A. Smolders, *J. Membr. Sci.* **1989**, *47*, 1; b) Y. Bessiere, N. Abidine, P. Bacchin, *J. Membr. Sci.* **2005**, *264*, 37.
- [30] P. Bacchin, D. Si-Hassen, V. Starov, M. J. Clifton, P. Aimar, *Chem. Eng. Sci.* **2002**, *57*, 77.
- [31] B. Espinasse, P. Bacchin, P. Aimar, *Desalination* **2002**, *146*, 91.
- [32] Q.-F. Liu, S.-H. Kim, *J. Membr. Sci.* **2008**, *310*, 393.
- [33] E. Iritani, N. Katagiri, T. Takenaka, Y. Yamashita, *Chem. Eng. Sci.* **2015**, *122*, 465.
- [34] P. H. Hermans, H. L. Bredée, *Recl. Trav. Chim. Pays-Bas* **1935**, *54*, 680.
- [35] a) V. E. Gonsalves, *Recl. Trav. Chim. Pays-Bas* **1950**, *69*, 873; b) H. P. Grace, *AIChE J.* **1956**, *2*, 307.
- [36] J. Hermia, *Trans. Inst. Chem. Eng.* **1982**, *60*, 183.
- [37] M. Hlavacek, F. Bouchet, *J. Membr. Sci.* **1993**, *82*, 285.
- [38] M. S. P. Shaffer, X. Fan, A. H. Windle, *Carbon* **1998**, *36*, 1603.
- [39] R. S. McLean, X. Huang, C. Khripin, A. Jagota, M. Zheng, *Nano Lett.* **2006**, *6*, 55.
- [40] L. Wu, B. Gao, Y. Tian, R. Muñoz-Carpena, K. J. Zigler, *Langmuir* **2013**, *29*, 3976.
- [41] C. Jiang, A. Saha, C. Xiang, C. C. Young, J. M. Tour, M. Pasquali, A. A. Martí, *ACS Nano* **2013**, *7*, 4503.
- [42] B. Dan, A. W. K. Ma, E. H. Haroz, J. Kono, M. Pasquali, *Ind. Eng. Chem. Res.* **2012**, *51*, 10232.
- [43] B. King, B. Panchapakesan, *Nanotechnology* **2014**, *25*, 175201.
- [44] N. Komatsu, M. Nakamura, S. Ghosh, D. Kim, H. Chen, A. Katagiri, Y. Yomogida, W. Gao, K. Yanagi, J. Kono, *Nano Lett.* **2020**, *20*, 2332.
- [45] E. M. Frohlich, J. L. Alonso, J. T. Borenstein, X. Zhang, M. A. Arnaout, J. L. Charest, *Lab Chip* **2013**, *13*, 2311.
- [46] J. S. Walker, J. A. Fagan, A. J. Bicchii, V. A. Kuehl, T. A. Searles, A. R. Hight Walker, W. D. Rice, *Nano Lett.* **2019**, *19*, 7256.
- [47] Z. Bi, Z. Zhang, F. Xu, Y. Qian, J. Yu, *J. Colloid Interface Sci.* **1999**, *214*, 368.
- [48] a) W. Gao, J. Kono, *R. Soc. Open Sci.* **2019**, *6*, 181605; b) R. Wang, J. Chen, L. Chen, Z. Ye, C. Wu, W. Gao, L. Xie, Y. Ying, *Desalination* **2020**, *494*, 114671; c) P.-H. Ho, D. B. Farmer, G. S. Tulevski, S.-J. Han, D. M. Bishop, L. M. Gignac, J. Bucchignano, P. Avouris, A. L. Falk, *Proc. Natl. Acad. Sci. USA* **2018**, *115*, 12662.
- [49] a) C. Huang, J. A. Wippold, D. Stratis-Cullum, A. Han, *Biomed. Microdevices* **2020**, *22*, 76; b) I. Pereiro, A. Fomitcheva Khartchenko, L. Petrini, G. V. Kaigala, *Lab Chip* **2019**, *19*, 2296.
- [50] X. H. Sun, D. M. Kanani, R. Ghosh, *J. Membr. Sci.* **2008**, *320*, 372.
- [51] a) V. G. J. Rodgers, R. E. Sparks, *J. Membr. Sci.* **1992**, *68*, 149; b) K. Nakamura, T. Orime, K. Matsumoto, *J. Membr. Sci.* **2012**, *401–402*, 274.
- [52] D. W. Green, R. H. Perry, in *Chemical Engineer's Handbook*, McGraw-Hill, New York **1999**.
- [53] a) N. Kuehn, H.-J. Jacobasch, K. Lunkenheimer, *Acta Polym.* **1986**, *37*, 394; b) C. Werner, U. König, A. Augsburg, C. Arnhold, H. Körber, R. Zimmermann, H.-J. Jacobasch, *Colloids Surf. A* **1999**, *159*, 519; c) S. Geissler, U. Werner, *Filtr. Sep.* **1995**, *32*, 533.
- [54] D. J. Miller, S. Kasemset, D. R. Paul, B. D. Freeman, *J. Membr. Sci.* **2014**, *454*, 505.
- [55] J. I. Calvo, A. Bottino, G. Capannelli, A. Hernández, *J. Membr. Sci.* **2004**, *239*, 189.
- [56] a) F. Yang, W. Wu, S. Chen, W. Gan, *Soft Matter* **2017**, *13*, 638; b) K. Suttiponparnit, J. Jiang, M. Sahu, S. Suvachittanont, T. Charinpanitkul, P. Biswas, *Nanoscale Res. Lett.* **2010**, *6*, 27.
- [57] B. White, S. Banerjee, S. O'Brien, N. J. Turro, I. P. Herman, *J. Phys. Chem. C* **2007**, *111*, 13684.
- [58] E. Iritani, *Drying Technol.* **2013**, *31*, 146.
- [59] a) P. van der Wal, U. Steiner, *Soft Matter* **2007**, *3*, 426; b) S. Alamri, A. I. Aguilar-Morales, A. F. Lasagni, *Eur. Polym. J.* **2018**, *99*, 27.
- [60] a) W. Zou, J. Sackmann, A. Striegel, M. Worgull, W. K. Schomburg, *Microsyst. Technol.* **2019**, *25*, 4185; b) A. Díaz Lantada, N. Mazarío Picazo, M. Guttman, M. Wissmann, M. Schneider, M. Worgull, S. Hengsbach, F. Rupp, K. Bade, G. R. Plaza, *Materials* **2020**, *13*, 1586.
- [61] P. Bacchin, A. Marty, P. Duru, M. Meireles, P. Aimar, *Adv. Colloid Interface Sci.* **2011**, *164*, 2.
- [62] H. Li, G. Gordeev, D. Toroz, D. Di Tommaso, S. Reich, B. S. Flavel, *J. Phys. Chem. C* **2021**, *125*, 7476.